JGR Solid Earth

RESEARCH ARTICLE

Special Collection:
Solid Earth Geophysics as a means to address issues of global change

Key Points:

- Poroelastic and statistical model suggests induced seismicity in Raton Basin is still primarily driven by wastewater injection
- Optimization reduces earthquake potential for a given amount of injected fluid or maximizes injection for a prescribed earthquake potential
- Optimization tends to spread out higher rate injection wells and may be a useful tool to reduce basin-scale induced earthquake potential

Supporting Information:

Supporting Information may be found in the online version of this article.

Correspondence to:

R. G. Hill,
rghill@lanl.gov

Mitigation and Optimization of Induced Seismicity Using Physics-Based Forecasting

Ryley G. Hill[1,2,3] ⓘ, Matthew Weingarten[1] ⓘ, Cornelius Langenbruch[4] ⓘ, and Yuri Fialko[2] ⓘ

[1]Department of Geological Sciences, San Diego State University, San Diego, CA, USA, [2]Scripps Institution of Oceanography, University of California San Diego, San Diego, CA, USA, [3]Now at Los Alamos National Laboratory, Los Alamos, NM, USA, [4]Institute of Geological Sciences, of Freie Universität Berlin, Dahlem, Germany

Abstract Fluid injection can induce seismicity by altering stresses on pre-existing faults. Here, we investigate minimizing induced earthquake potential by optimizing injection operations in a physics-based forecasting framework. We built a 3D finite element model of the poroelastic crust for the Raton Basin, Central US, and used it to estimate time dependent Coulomb stress changes due to ~25 years of wastewater injection in the region. Our finite element model is complemented by a statistical analysis of the seismogenic index (SI), a proxy for critically stressed faults affected by variations in the pore pressure. Forecasts of seismicity rate from our hybrid physics-based statistical model suggest that induced seismicity in the Raton Basin, from 2001 to 2022, is still driven by wastewater injection despite declining injection rates since 2011. Our model suggests that pore pressure diffusion is the dominant cause of Coulomb stress changes at seismogenic depth, with poroelastic stress changes contributing about 5% to the driving force. Linear programming optimization for the Raton Basin reveals that it is feasible to reduce earthquake potential for a given amount of injected fluid (safety objective) or maximize fluid injection for a prescribed earthquake potential (economic objective). The optimization tends to spread out high-rate injectors and shift them to regions of lower SI. The framework has practical importance as a tool to manage injection rate per unit field area to reduce induced earthquake potential. Our optimization framework is both flexible and adaptable to mitigate induced earthquake potential in other regions and for other types of subsurface fluid injection.

Plain Language Summary The Raton Basin, in the central United States, has had a remarkable increase in seismicity coincident with large wastewater injection since 2001. This seismicity primarily occurs at depths greater than several kilometers where preexisting faults in the crystalline basement are reactivated by increasing pore pressure due to fluid diffusion. The spatial extent and rate of the induced earthquakes can inform earthquake probability maps which display the probability of an earthquake occurrence within a specific time period. We use the physics-based and statistical models to develop an optimization framework that may help inform well operations. The proposed method allows for the maximization of injected fluid (the economic objective) and the reduction of earthquake potential (the safety objective).

1. Introduction

Induced seismicity is a growing problem world-wide as it accompanies a variety of industrial activities, including hydraulic fracturing (Bao & Eaton, 2016; Rutqvist et al., 2015) and wastewater disposal (Ellsworth, 2013; Keranen et al., 2014; Shirzaei et al., 2016), extraction and storage of natural gas (Grasso & Wittlinger, 1990; van Thienen-Visser & Breunese, 2015; Zbinden et al., 2017), CO_2 sequestration (Goertz-Allmann et al., 2014; White & Foxall, 2016), and renewable geothermal energy exploitation (Fialko & Simons, 2000; Giardini, 2009; Majer & Peterson, 2007; Mignan et al., 2015). Within the last decade, a dramatic increase in seismic activity in the Central and Eastern United States (CEUS) was caused by deep injection of water that was co-produced with oil (Keranen et al., 2014; Langenbruch et al., 2018; Langenbruch & Zoback, 2016; Walsh & Zoback, 2015). Several moderate (M5+) events were induced in historically aseismic regions (Ellsworth, 2013; Foulger et al., 2018; Weingarten et al., 2015). Like natural tectonic earthquakes, induced events occur on pre-existing critically stressed faults, primarily in the crystalline basement (Townend & Zoback, 2000).

The occurrence of induced seismicity is attributed to various physical mechanisms, including pore pressure diffusion, poroelastic coupling, stress changes caused by seismic or aseismic fault slip, and stressing due to tensile hydraulic fracture opening (Ge & Saar, 2022; Keranen & Weingarten, 2018; Kettley et al., 2020; Moein

et al., 2023; Segall & Lu, 2015). In general, all mechanisms may contribute to the triggering of seismicity, because induced earthquakes can be triggered by stress changes just above stress perturbations caused by the Earth's tides (1–10 kPa) (Bachmann et al., 2012; Cacace et al., 2021; W. Wang et al., 2022; Stokes et al., 2023). Modeling studies at well-characterized injection locations show that the relative significance of these mechanisms varies from site to site depending on the physical rock properties, reservoir structure, fault geometry, seismotectonic conditions, and distance from injection among others (Keranen & Weingarten, 2018; Segall & Lu, 2015; Weingarten et al., 2015; Zhai et al., 2019). Pore pressure diffusion and poroelastic stress changes are considered primary mechanisms for induced seismicity (Ge & Saar, 2022; Keranen & Weingarten, 2018; Segall & Lu, 2015; Stokes et al., 2023; Zhai et al., 2019).

Understanding and mitigating the seismic response to fluid injection is still a major challenge, not just for wastewater disposal, but for other types of subsurface fluid injection: CO_2 sequestration, enhanced geothermal systems and hydraulic fracturing. In each region where subsurface fluid injection occurs, it is paramount to future operations to find an optimal balance of efficient yet safe injection practices. The field of hydrogeology has long used coupled groundwater simulations and management models to optimize pressure changes in multiple wells for a certain benefit (Gorelick, 1983; Gorelick & Zheng, 2015). For example, Gorelick and Remson (1982) sought the optimal solution that maximized pollutant disposal while meeting spatial water quality standards at the wells over time. A similar approach for wastewater injection and induced seismicity could involve maximizing injection rates while adhering to spatial constraints to prevent fault reactivation.

Here, we present a framework that seeks to optimize the amount of wastewater injected at the basin-scale with a fully coupled poroelastic model combined with a statistical seismicity forecasting model. Optimization is performed under a spatially varying Coulomb failure stressing rate constraint dependent on faulting orientation (King et al., 1994; Cocco & Rice, 2002; Z. Jin et al., 2022). We first demonstrate the hybrid model's effectiveness at forecasting the observed seismicity in the Raton Basin of Colorado and New Mexico—a long-standing and well-documented case of induced seismicity. We then demonstrate the feasibility of future induced seismicity management using optimization of injection under various constraint scenarios.

For our simulation and management models, we take advantage of the linearity in the fully coupled poroelastic equations as well as the linearity in the Coulomb stress equation. Coupled poroelastic calculations are performed using a 3D finite element hydromechanical model (Dassault Systemes, 2020). Our statistical seismicity model follows the methodology of prior work performed in Oklahoma and Kansas, where spatiotemporal variations of induced earthquake potential are calculated from pore pressure changes and spatial variations of the subsurface's susceptibility to induced earthquakes (Langenbruch et al., 2018). The susceptibility is described by the spatially varying seismogenic index (SI), a proxy for the number and stress state of pre-existing basement faults affected by stress changes (Langenbruch & Zoback, 2016; Shapiro et al., 2010). Note that the SI model applied in Oklahoma and Kansas only considered pore pressure changes, while we consider the fully coupled problem by including poroelastic stress changes in the Coulomb stress analysis. We then form a management model using a response matrix for rate dependent model constraints provided by the SI.

The management models considered are three 5-year prospective scenarios that use the remnant pore pressure and stress conditions from prior injection in the Raton Basin. In each scenario, the optimization chooses which injection wells to operate and at which monthly rate of injection. The first scenario optimizes induced earthquake potential for an injection strategy that tapers the overall injection by 70% from the 2022 levels (reduction objective). The second scenario minimizes the earthquake potential for the current Raton Basin injection rate, thus optimizing earthquake potential for a given injected volume (safety objective). The third scenario maximizes the total injected volume while holding constant Raton Basin's currently forecasted earthquake potential (economic objective). The total framework serves as a flexible platform by which the optimization of injection activities are drafted to reduce the earthquake potential and maximize an economic objective.

1.1. Raton Basin

The Raton Basin, a ~150 km long by ~75 km wide sedimentary basin situated along the border between Colorado and New Mexico, has shown a remarkable seismic rate increase coincident with the beginning of industrial-scale wastewater injection in 2001 (Rubinstein et al., 2014) (Figure 1). The source of the wastewater is from coal-bed methane production from the Raton and Vermejo formations (Nakai, Weingarten, et al., 2017). The rate increase was punctuated by the 23 August 2011 M5.3 Trinidad, Colorado earthquake, which caused structural damage in
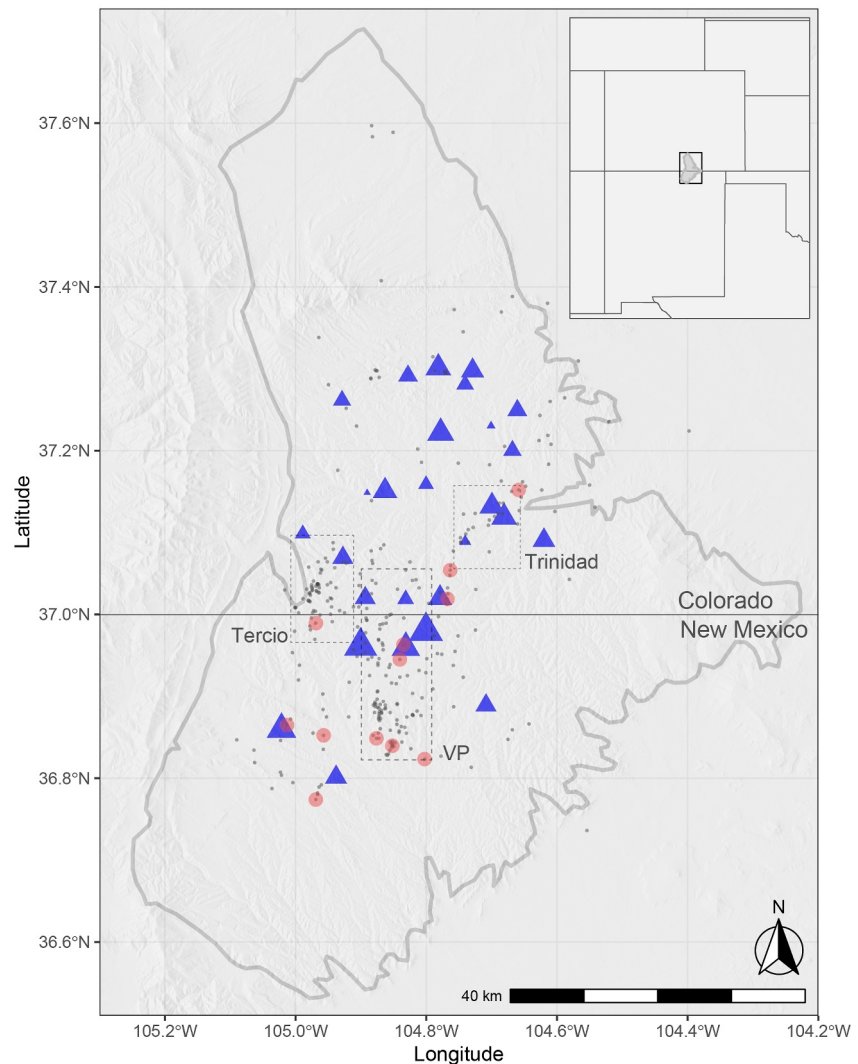
Figure 1. Regional Context. Light gray outline is the Raton Basin. Blue triangles are the 29 injection wells sized as per cumulative volume injected from Nov-1994 to May-2022. Gray dots are earthquakes with M≥2.5 and red dots are earthquakes with M≥4 from Nov-2001 to July-2020. Boxed regions represent zones of seismicity: Tercio, Vermejo Park, and Trinidad.

the nearby town of Trinidad, as well as 17 M4+ events, the most recent of which occurred on 10 March 2023 [ANSS Comprehensive Catalog] (Figure 1). Previous studies have linked seismicity and wastewater injection wells operating in the basin using observational evidence and physical modeling (Barnhart et al., 2014; Nakai, Weingarten, et al., 2017; Rubinstein et al., 2014). The time-dependent earthquake potential associated with these induced events can change based on the pumping rates associated with the injection wells. Understanding both the spatial and temporal change of past earthquake potential is critical to mitigating future hazard.

Injection induced seismicity began in 2001 and peaked in late 2011 with the 23 August 2011 M5.3 Trinidad, Colorado earthquake (Figure 2). Since 2011, regional injection rates have declined more than ~33%, but the basin continues to exhibit an elevated seismicty rate with several recent M4+ events (Glasgow et al., 2021b). The regional stress field is heterogeneous, with a substantial rotation of the maximum horizontal stress from predominantly north-south to east-west directions (Snee & Zoback, 2022). The earthquake focal mechanisms indicate a mixture of normal and strike-slip earthquakes (R. Wang et al., 2020; Glasgow et al., 2021b).

Geologic and hydrogeologic data show that the Dakota-Purgatoire Formation, a fractured sandstone reservoir, and the underlying Glorieta sedimentary units are permeable and hydraulically connected across a large area of
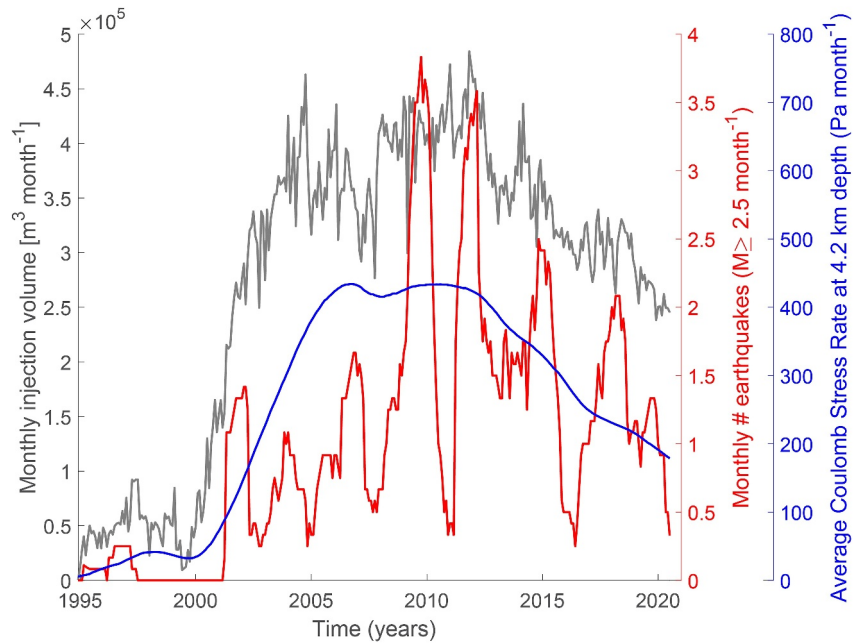
Figure 2. Injection, induced earthquakes, and Coulomb stress rate. Total monthly injection volume (gray), observed earthquakes M≥2.5 (1 year moving mean), and the average modeled Coulomb stress rate in the study area. The Coulomb stress rate lags the injection rate due to the diffusion of pore pressure into the crystalline basement. A correlation between increased stress at depth and seismicity is observed.

the basin (Geldon, 1989; Nelson et al., 2013). Pennsylvanian and Early Permian Sangre de Cristo sediments lie beneath the Glorieta, separating the wastewater disposal interval from the Precambrian basement by ~1.2 km (Belitz & Bredehoeft, 1988). The injection reservoir is also well-confined from the shallower stratigraphy within the basin by more than 700 m of poorly permeable Pierre Shale. Additionally, the western boundary is characterized by the Sangre de Cristo Mountain thrust fault system, a complex of west-dipping, Laramide-age thrust faults that show dip-slip offsets of 0.6–3 km (Clark et al., 1966). The observed seismicity in the Raton Basin is primarily found within the crystalline basement at average depths of 5–7 km below surface (Glasgow et al., 2021b; Nakai, Weingarten, et al., 2017). There is also strong evidence to suggest three prominent zones of seismicity: Tercio, Vermejo Park, and Trinidad (Figure 1) (Barnhart et al., 2014; Higley, 2007; Macartney & O'Farrell, 2010).

2. Physics-Based Forecasting Model

2.1. Methods

2.1.1. Linear Poroelasticity

To understand how injection across the Raton Basin is changing stress on pre-existing basement faults, we develop a fully coupled poroelastic model and compute the Coulomb stress changes at depth. Linear poroelasticity is essential to understanding the time-dependent coupling between the deformation of, and fluid flow in, hydrogeologic units within the Earth. The governing equations for a fully coupled linear poroelastic three-dimensional medium are defined as (Biot, 1941; Rice & Cleary, 1976; H. Wang, 2000):

$$G\nabla^2 u_i + \frac{G}{1-2\nu}\frac{\partial^2 u_k}{\partial x_i \partial x_k} = \alpha\frac{\partial P}{\partial x_i} - F_i, \tag{1}$$

$$\alpha\frac{\partial \epsilon_{kk}}{\partial t} + S_\epsilon\frac{\partial P}{\partial t} = \frac{k}{\mu}\nabla^2 P + Q, \tag{2}$$

where G is the shear modulus, u the displacement, ν the Poisson's ratio, α the Biot-Willis coefficient, F the body force, k the permeability, μ the fluid viscosity, S_ϵ the constrained specific storage, ϵ_{kk} the volumetric strain, P the pore pressure, and Q the fluid source (H. Wang, 2000). Equation 1 are nearly identical to the classic equations for linear elasticity except for the coupling of pore pressure in the conservation of linear momentum Equation 1 and the fluid flow coupled to strain by the requirement of fluid continuity (2). However, system (1)–(2) is more difficult to solve, with analytic solutions restricted to a few highly idealized cases. We solve the respective equations numerically using the three-dimensional finite element software Abaqus FEA (Dassault Systemes, 2020; Hill et al., 2023; LaBonte et al., 2009; Pearse & Fialko, 2010). We validate the robustness of the numerical solution provided by Abaqus by summarizing its equivalency to that of a linear poroelastic framework (Jin, 2023; Jin et al., 2023). Additionally, we resolve the numerical pore pressure and stress outputs of a fluid mass point source compared with an analytical solution as further validation that Abaqus is a robust linear poroelastic framework (Rudnicki, 1986) (see SM Section 1).

The pore pressure diffusion is governed by an inhomogeneous diffusion equation Equation 2. Because the fluid flow is coupled with the strain field, pore pressure changes have direct effects on the stress and changes in the strain have direct effect on the fluid pressure. Under different assumptions, the stress field will uncouple from the pore pressure field and the diffusion equation resembles its hydrogeologic counterpart; the ground water flow equation $S \frac{\partial P}{\partial t} = \frac{k}{\mu} \nabla^2 P + Q$ (where $S = S_\epsilon \frac{K_v^{(u)}}{K_v}$) (Detournay & Cheng, 1993; H. Wang, 2000).

Following Gorelick and Remson (1982) and Gorelick et al. (1993), we use a physics-based numerical model to generate a unit source response matrix (see Section 3.1.2). The key difference is that our simulation model incorporates the fully coupled poroelastic response (1–2), calculated using a finite element model, and generates a unit source response matrix of Coulomb stress (3) which is only possible due to the linearity in all the equations. The Coulomb stress is also dependent on fault geometries (SM Figure 1 in Supporting Information S1).

2.1.2. Stressing Rate and Earthquake Probability

Triggering of seismic events due to fluid injection can be adequately described by Equations 1 and 2 and changes in Coulomb stress (H. Wang, 2000; Cocco & Rice, 2002). Coulomb stress τ is defined as:

$$\tau = \tau_s + \mu(\sigma_n + P), \tag{3}$$

where τ_s is the shear stress on a fault plane, σ_n is the normal stress (compression is deemed negative), P is the pore pressure, and μ is the coefficient of friction. An increase in pore pressure reduces the absolute value of the effective stress ($\sigma_e = \sigma_n + P$) such that the Coulomb stress increases, corresponding to promotion of failure. In the presence of a regional stress field even modest perturbations in pore pressure may encourage slip on pre-existing critically stressed faults. The diffusion of pore pressure is highly dependent on hydraulic properties. Furthermore, depending on fault geometries, the poroelastic coupling of the fluid may play a significant role in promotion or inhibition of fault failure, especially in the far field where the effects of fluid percolation are negligible (Segall & Lu, 2015).

Similar to previous work (Langenbruch et al., 2018), which was carried out in the region of north-central Oklahoma and southernmost Kansas, seismicity data in the Raton Basin also shows the expected increase of earthquake probability with the rate of stress increase (Supplementary Methods). These observations can be used to describe the monthly earthquake rates $R_{\geq M}(r, t)$ according to a modified Gutenberg-Richter law for induced earthquakes (Langenbruch et al., 2018):

$$R_{\geq M}(\boldsymbol{r}, t) = 10^{a(r,t)-bM} = \left[\frac{\partial}{\partial t}\tau_\tau(\boldsymbol{r}, t)\right]^2 10^{\Sigma_\tau(r) - \boldsymbol{b}M}, \tag{4}$$

Here, we replaced the pore pressure rate, used by (Langenbruch et al., 2018) by the monthly Coulomb stressing rate $\frac{\partial}{\partial t}\tau_\tau(\boldsymbol{r}, t)$ in space and time to add the effect of poroelastic coupling. $\Sigma_\tau(\boldsymbol{r})$ is the spatially varying Seismogenic Index (SI). The SI and b values are evaluated through a specific calibration period (see Section 2.3). The calibrated parameters are then used to forecast expected earthquake rates and to initialize the management model (see Section 3) for optimization. An important distinction from previous studies (Langenbruch et al., 2018) is the use
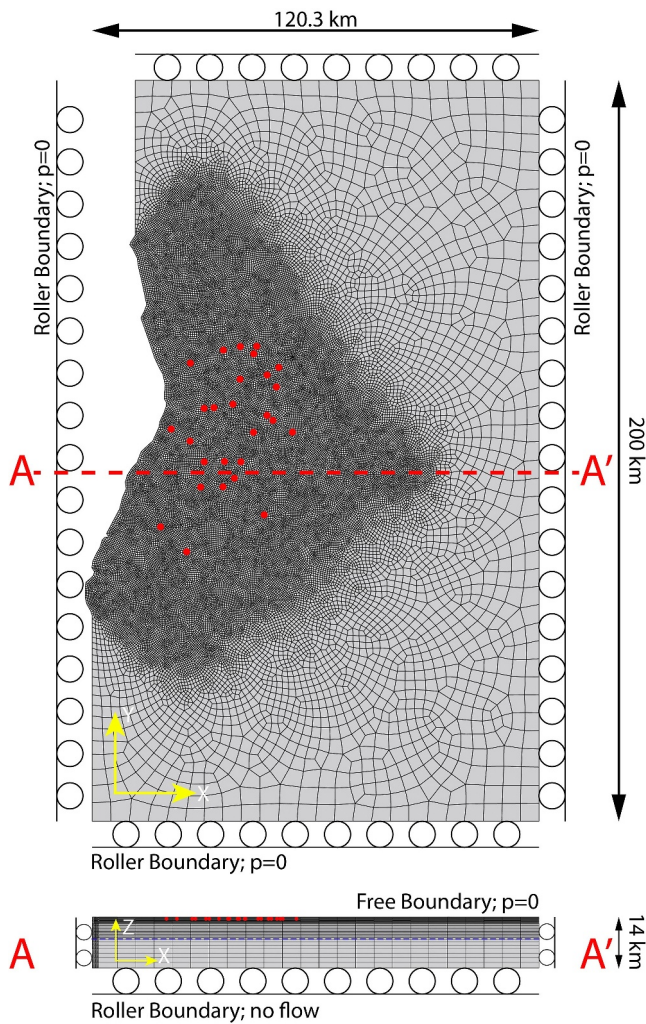
Figure 3. Numerical Domain. Three-dimensional finite-element model domain. The model mesh contains about 1.5 million hexahedron elements. The Red dots represent the well injection locations. The blue dotted line represents pore pressure and stress output location at the mean seismogenic depth (~7 km depth or 4,240 m below the top of the crystalline basement).

of Coulomb stressing rate $\frac{\partial}{\partial t}\tau_\tau(\mathbf{r}, t)$ as opposed to pressure rates. While pore pressure rates are still the dominant signal (SM Figure 2 in Supporting Information S1), the fully coupled numerical model takes into account the full stress field.

2.2. Numerical Domain

The numerical domain was developed and discretized in Abaqus CAE (Complete Abaqus Environment, Dassault Systemes, 2020). The domain has horizontal dimensions of 120 km × 200 km and a depth dimension of 14 km, with the y axis corresponding to north in the Universal Transverse Mercator coordinates (Figure 3). The finite-element mesh consists of nearly 1.5 million first-order hexahedral elements. Characteristic element sizes vary from 5,000 m in the far field to less than 500 m near the injection wells and in the vicinity of the central basin. The depth domain is partitioned into the five distinct hydrogeologic layers of the basin. The heterogeneous hydrogeologic properties of the model are summarized in Table 1. Permeability and storage parameters of the primary injection formations, the Dakota-Purgatoire and Morrison-Glorieta, were calibrated from analysis of injection step-rate tests (see Supplementary Materials in Supporting Information S1). The permeability k of the Dakota-Purgatoire formation and the Morrison-Glorietta formation is taken to be 6.4–6.8 ×10^{-14} and 5.8–8.9 ×10^{-14} m^2, respectively. While no wells penetrate the crystalline basement for diagnostic analysis of basement permeability, we chose a crystalline basement permeability ($k = 1 \times 10^{-15}$ (m^2)) that results in the best correlation between the observed seismicity rates and modeled pressure rates (Figure 2). While this permeability is slightly higher than that measured in small-scale laboratory experiments and inferred for basement rocks in some regions (Brace, 1980; H. Wang, 2000; Shmonov et al., 2003; Ross et al., 2020), it is similar to large-scale basin estimates made in regions of induced seismicity (Langenbruch et al., 2018; Nakai, Weingarten, et al., 2017). In addition, it is also consistent with constraints on in situ hydraulic diffusivity of the upper crust from observations of post-seismic deformation (e.g., Fialko, 2004). The increased permeability is chosen to capture the basin-scale permeable faults that transmit fluid pressure to seismogenic depths (Caine et al., 1996; Hill et al., 2023).

We assume initial conditions of equilibrium stress and pore pressure (Segall, 2010, chapter 9). Therefore, the model only considers the perturbing effects of the wastewater injection and does not include any tectonic loading.

Table 1
Material Properties

Unit	Pierre-benton-niobrara	Dakota-purgatoire	Morrison-entrada-gloreita	Sangre de cristo	Crystalline basement
Depth (km)	1–1.4	1.4–1.6	1.6–2	2–2.8	2.8–15
Thickness (m)	400	200	400	800	1,220
Permeability (m^2)	$1 \cdot 10^{-20}$	$6.7 \cdot 10^{-14}$	$8.9 \cdot 10^{-14}$	$8 \cdot 10^{-15}$	$1 \cdot 10^{-15}$
E (GPa)	0.22	38	32	40.74	60
v	0.3	0.287	0.13	0.15	0.25
K_s (GPa)	0.34	33.8	26.6	36.6	42
ϕ	0.38	0.25	0.07	0.06	0.01

Note. Hydrogeologic material values for different units and their corresponding depths in the numerical model. Note that the model begins at 1 km depth below the surface.
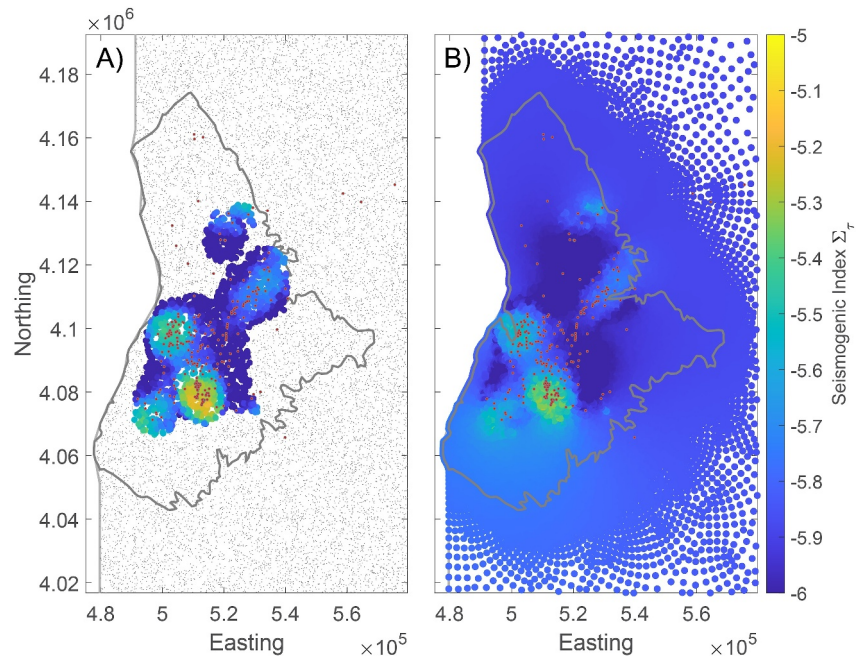
Figure 4. Seismogenic Index Σ_τ Maps. Mapped spatial variability of the SI in the Raton Basin. The SI is computed in local regions of 7-km radius around the 25,000 seed points (gray dots in panel A). The calibration time is between Nov-1994 and July-2016. See Methods for additional details. Red dots represent earthquakes M≥2.5 used in calibration. Panel (b) represents the inverse distance weighted interpolation of the SI to the model points used in the forward model management solutions.

The bottom and sides of the model are fixed only in the surface normal direction (the roller boundary condition). The top surface of the model is stress-free. We model the Sangre de Cristo Mountain complex of thrust faults as barriers to cross-fault fluid flow and use an insulating condition at the western boundary of the model. We use the same injection depth of 1,500 m for all wells as the former is the middle depth of the modeled Dakota-Purgatoire injection reservoir. We record pore pressure and stress perturbations at the mean seismogenic depth of ~7,040 m which is equivalent to ~38,000 observation points for each time step. Generation of the SI map requires the full 29 well injection profile data ranging from November 1994 to May 2022, giving rise to 331 monthly time steps, while the 5 years response matrix models require only 61 time steps.

2.3. Seismogenic Index (SI)

The SI map is a map of the seismo-tectonic state controlled by the number and stress state of pre-existing faults in the crystalline basement affected by Coulomb stress changes (Figure 4) (Langenbruch et al., 2018). The SI ($\Sigma_\tau(r)$) is determined in local regions of 7 km radius at ~25,000 seed points. The seed points represent the interpolated Coulomb stress changes produced by the model at the mean seismogenic depth within the crystalline basement. The higher the SI ($\Sigma_\tau(r)$) at each seed point, the higher the earthquake rate caused by a given Coulomb stress increase, because a higher number of (or more critically stressed) preexisting faults are affected by the Coulomb stress increase (see Equation 4).

Calibration of the SI is set based on a calibration time period. In this way, future modeled Coulomb stressing rates are used to forecast expected spatiotemporal earthquake rate. We set the calibration time (Nov 1994 to July 2016) of our SI map prior to the Glasgow et al., 2021b study and find that forecasted earthquakes (July 2016 to July 2020) are well explained by basin Coulomb stressing rate, despite lowered injection rates at this time (Figure 6).

Calibration of SI follows closely to previous methods (Langenbruch et al., 2018). The following steps are performed to calibrate the SI maps.
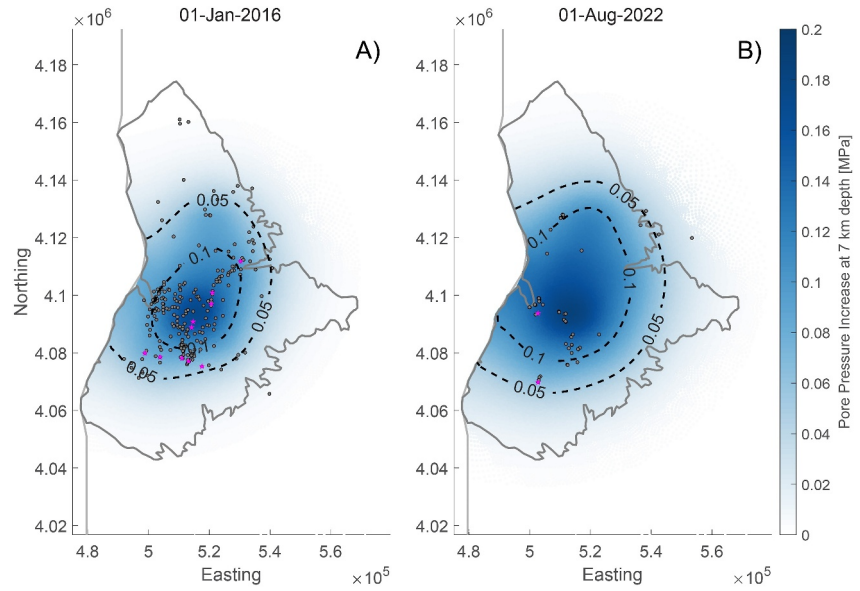
Figure 5. Pore Pressure Increase. (a) Pore pressure increase at mean seismogenic depth across the basin including seismicity from Aug 2001 to Jan 2016. Black dots represent earthquakes with M≥2.5+ and magenta stars are earthquakes with M≥4+. (b) Pore pressure increase at mean seismogenic depth across the basin including seismicity from Jan 2016 to Aug 2022.

1. Monthly Coulomb stressing rates $\frac{\partial}{\partial t}\tau_\tau(\boldsymbol{r_n}, t)$ at all n seed points with a radius of 7-km around a selected seed point up to a given calibration time t_c (we use Nov-1994 to July-2016) are extracted, squared, and summed $\sum_n \left[\frac{\partial}{\partial t}\tau_\tau(\boldsymbol{r_n}, t \leq t_c)\right]^2$

2. The total number $N_{M \geq M_c}(t \leq t_c)$ ($M_c = 2.5$, see SM Figure 3 in Supporting Information S1) of earthquakes within a 7-km radius around the current seed point observed up to the given calibration time is summed.

3. Estimate of the b-value is computed using all $M \geq M_c$ earthquakes recorded through the calibration time t_c in the complete study area.

4. The SI at location $\boldsymbol{r}$ is evaluated:

$$\Sigma_\tau(\boldsymbol{r}) = \log_{10} N_{M \geq M_c}(t \leq t_c) - \log_{10}\left\{\sum_n \left[\frac{\partial}{\partial t}\tau_\tau(\boldsymbol{r_n}, t \leq t_c)\right]^2\right\} + b(t_c)\, M \tag{5}$$

Due to the occurrence of singular earthquakes outside of the local areas of elevated seismicity one can get outlier SI values. These events are often attributed to Coulomb stressing rates that are quite low which results in significantly larger than average SI at those locations. Prior work found that as soon as two earthquakes occurred within the chosen radius of any given seed point a good estimate of the SI can be obtained (Langenbruch et al., 2018). Our region uses a smaller radius and calibration magnitude. Therefore, we precondition the SI to only be evaluated when there are more than three earthquakes. We evaluate the sensitivity of the SI for different calibration periods (SM Figure 4 in Supporting Information S1) which produce minor differences. We also evaluate sensitivity due to a smaller 5-km radius and removal of the "more than three earthquakes" precondition. These changes produce an SI map that appears different, as outliers are now included, but the overall seismicity rate remains very similar (SM Figures 5 and 6 in Supporting Information S1).

Within the central basin region, we find that the SI varies by about 1.5 units (Figure 4). A one unit increase in SI is the equivalent of expecting 10 times more earthquakes for the same CFS rate change at that location. A higher SI in the central basin corresponds spatially with the well known zones of seismicity: Tercio, Vermejo Park, and Trinidad.

The SI is dependent on the spatial density of the observed seismicity and the radius of inclusion. This implies that seed points without observed seismicity in a 7-km radius will not produce SI. For the purpose of forecasting seismicity and optimizing injection rates for the entire basin we use an inverse distance weighting interpolation
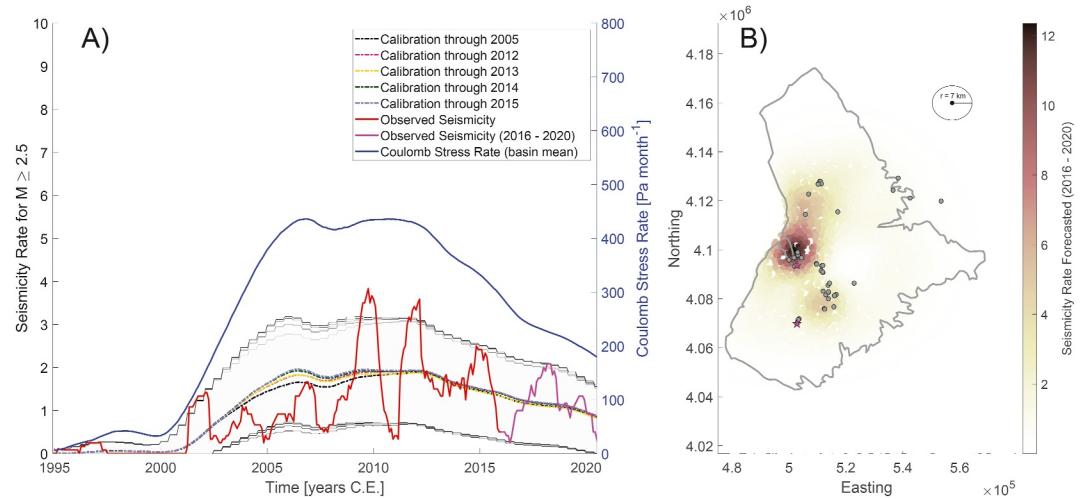
Figure 6. Seismicity Rate Forecast. (a) Seismicity rate forecasts, above our completeness magnitude M≥2.5, compared to observed seismicity rate (1 year moving mean). Calibration period is from Nov 1994 through 2005, 2012, 2013, 2014, 2015, and 2016 prior to the Glasgow et al., 2021a study (Glasgow et al., 2021b). The earthquakes and longest calibration time period used to calibrate the SI model is represented by the red line. The varying dashed lines and gray boundaries are the 95% confidence bounds forecasted by the seismicity rate produced from the SI model that includes the inverse distance weighted interpolation (right panel of Figure 4). Magenta line represents the observed seismicity from Glasgow et al., 2021a which is well explained by the seismicity rate forecasted by our model. (b) Spatial seismicity rate forecast for 2016–2020 associated with the magenta line in panel a using a 7 km radius summation. Observed earthquakes are plotted as gray circles and M≥4+ are plotted as magenta stars. Visual inspection shows good agreement between spatially forecasted seismicity rate and observed earthquakes.

(power = 2, radius = ∞) (Figure 4) in areas that have no observed seismicity during the calibration period. The smoothing maintains local heterogeneity while populating areas with otherwise no SI. The central basin has the lowest SI because it has high stress changes without causing seismicity, while areas farther away have higher SI due to lower stress changes that still induce seismicity. The interpolated map helps inform the Coulomb stressing constraints in the SI dependent response matrix models. The basin-scale interpolation allows short calibration periods (2005) to forecast the seismicity rate in the model well (Figure 6). While the overall basin-scale seismicity is not very sensitive to calibration, the spatial optimization (Section 3) is much more dependent on the spatial aspects of the SI.

The SI is also dependent on the stressing rate, which is primarily a function of the pore pressure (SM Figure 2 in Supporting Information S1), that is sensitive to uncertainty in the model permeability. Treating the numerical model with a laterally homogeneous permeability allows the SI to capture areas of preexisting critically stressed faults without any bias to permeability uncertainty. Since an increase/decrease in the permeability will increase/ decrease stressing rate during seismicity the SI is affected. Generally, the SI would still accommodate these changes in a relative sense. For example, if across the basin the stressing rates were all lower during seismicity due to a reduction in permeability, the overall SI would be higher since a low pressure rate was still producing the same amount of seismicity. There is evidence of permeable faults potentially acting as hydraulically connected pathways in the Raton Basin (Nakai, Weingarten, et al., 2017; Rubinstein et al., 2014). Lateral heterogeneity in permeability uncertainty is beyond the scope of this work. However, the approach to include uncertainty in the permeability, or any material parameter, is possible (see Section 7.4).

2.4. Results and Discussion: Forecast Performance (2016–2020)

The results of the time dependent pore pressure evolution and associated seismicity during our calibration time are shown in Figure 5. The pore pressure continues to increase at depth within the basin due to the diffusion of fluid pressure despite lowered injection rates during 2016–2022. The total pore pressure increases, but the rate of increase declines (Figure 2). Returning to Equation 4, we can now forecast seismicity rate beyond our calibration time using both the SI map and Coulomb stress perturbations from the numerical model. Figure 6 depicts the seismicity rate forecasts from a variety of calibration time periods and the resulting projected seismicity rate
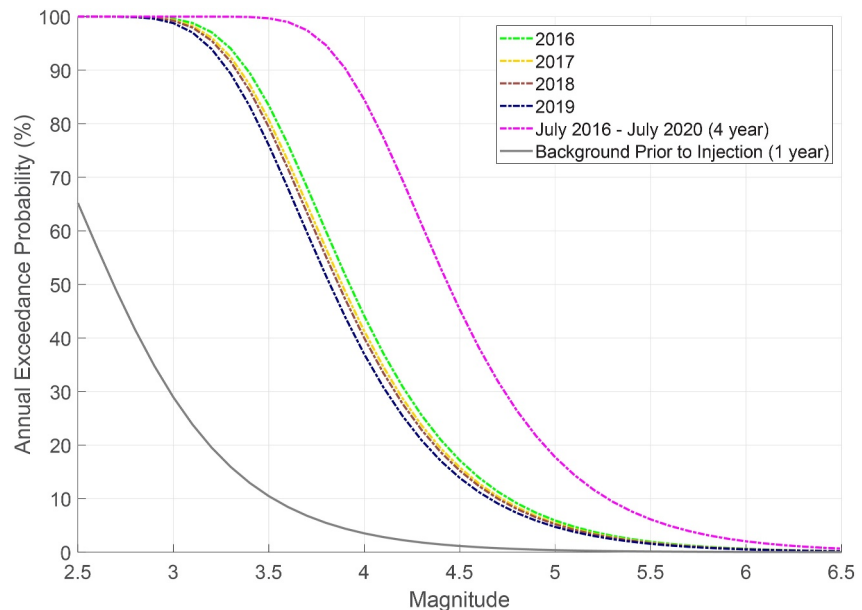
Figure 7. Forecasted Magnitude Exceedance Probabilities. Exceedance probabilities for magnitudes M≥2.5–6.5 from our physic-based forecasting model. Each line represents the probability forecasted by our model based on the calibrated SI map and computed Coulomb stress model outputs. The forecasted probability from 2016 to 2020 is significantly higher than the tectonic background (gray line) and is highest in 2016. Background probabilities are derived from prior work (Rubinstein et al., 2014). Each year from 2016 to 2019 the magnitude exceedance probabilities or decreasing, but still above the tectonic background level. From 2016 to 2020 the potential to trigger a M≥5+ increases to ∼18%.

between 2016 and 2020. There is little sensitivity of the modeled earthquake rates to the calibration time. We find that the observed seismicity rate from 2016 to 2020 fits well by our calibrated SI model and the computed Coulomb stress changes (Figure 6 and SM Figure 9 in Supporting Information S1). We further validate the seismicity forecast by comparing the joint log-likelihood scores of our forecast to both a spatially uniform and more heterogeneous uniform random seismicity model. Each forecast is rate normalized so that total seismicity is not considered in the performance. The results of the joint log-likelihood scores indicate our model outperforms both the spatially uniform and uniform random seismicity rate models (SM Figures 7–8 in Supporting Information S1).

Furthermore, assuming the occurrence of induced earthquakes follows a Poisson process (Langenbruch et al., 2011; Langenbruch & Zoback, 2016; Shapiro et al., 2010), the probability of exceeding a magnitude *M*, that is the probability to observe one or more events of magnitude *M* or larger, is given by (Langenbruch et al., 2018):

$$\Pr(M) = 1 - \Pr(0, M, N_{\geq M}) = 1 - \exp(-N_{\geq M}) \tag{6}$$

Where, $(N_{\geq M})$ is the expected number of events of magnitude *M* or larger in a considered time interval (see Equation 4).

Based on our calibrated model, we compute the annual expected number of events in the range from *M* 2.5–6.5 and determine magnitude exceedance probabilities using Equation 6 (Figure 7). Our results suggest that between 2016 and 2020 there was a ∼85% probability to observe one or more M≥4+ earthquakes and a ∼18% probability to observe one M≥5+. We find good agreement with earthquake count for the forecasted seismicity and the observed seismicity (SM Figure 9 in Supporting Information S1). We find that Coulomb stress rates at seismogenic depth continued to trigger seismicity between 2016 and 2020 although injection rates declined. Therefore, induced seismicity was still driven by wastewater injection during this time period. Declining injection rates alone are not necessarily an indicator of decreased earthquake potential as one must also consider diffusion-driven time delays in the induced seismicity process.
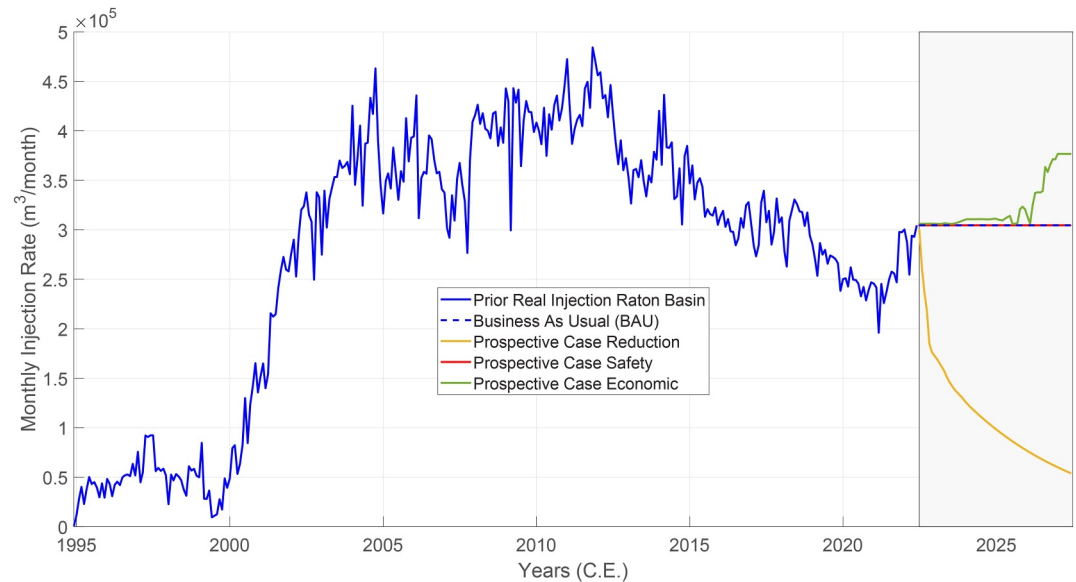
Figure 8. Different Optimization Scenarios. Plot shows the monthly injection rate (total of all 29 wells) for the observed data (blue). At June-01-2022, the next 5 years window (gray box) represent the forecasted injection rates. The business-as-usual rate takes the last known injection rates and holds them constant for the 5 years (blue-dash). The prospective case 'Reduction' is the optimized injection rates subject to reducing the overall injection by 70% in 5 years as well as a taper in individual well rates (yellow). The prospective case 'Safety' is the optimized injection rates subject to the constraint that the total fluid injected must be the same as the BAU, but reduces the overall earthquake potential (Figure 9) (red). The prospective case 'Economic' is the optimized injection rates subject to the constraint that the overall 5 years earthquake potential must be the same as the BAU, but increases the overall injection (green).

2.5. Results and Discussion: Business as Usual Forecast (2022–2027)

In this section we explore the seismicity forecasted by our calibrated model from 2022 through 2027 under a hypothetical 'business as usual' (BAU) injection scenario. The BAU scenario uses the last observed monthly injection rate for each well from May 2022 and holds them constant until May 2027 (Figure 8). It should be understood that this is not an ideal forecast of the observed seismicity during this time since the forecasted injection rates are not the real injection rates which are unknown. Instead, this scenario represents a hypothetical informed estimate and serves as a baseline for comparison with the optimization models discussed in Section 3. We list the following important results of the BAU forecast.

- The BAU forecast from 2022 to 2027 shows that the probability to exceed a M≥5+ event is ~15% and a M≥4+ event is ~75% (Figure 9).
- Spatially, higher rate injection wells are clustered in the central portion of the basin near the Vermejo Park cluster. Injection wells in this area, just south of the CO-NM border, on average inject at rates higher than 20,000 m^3 per month (Figure 10(B)).
- Earthquake potential is also mostly elevated in this same region for the BAU forecast (Figure 10(A)). Within this region of clustered injection, the spatial probability to exceed a M≥4+ is ~20% over the 5-year BAU forecast.
- Earthquake potential in the North of the basin is proportionally smaller. We interpret this as a result of lower injection rates, largely below ~10,000 m^3 per day, and lower SI in this region.
- The two observed M4+ events that have occurred from May 2022 to September 2023 occur within the zone of elevated earthquake potential forecasted by our model (Figure 10)
- In comparison to a complete shut-in of injection in May 2022, BAU injection increases the likelihood of a M≥4+ event by 150% (from 30% to 75%) and a M≥5+ by more than 200% (from 5% to 15%) (Figure 9).

SM Figures 10–11 in Supporting Information S1 show the seismicity rate forecasts resulting from the BAU projected injection rates. The forecasted seismicity rates are used to produce magnitude exceedance probabilities from our calibrated SI model (Figure 9). Figure 9 also includes the lower bound on any optimization we can achieve, the shut-in scenario, which represents the post-diffusion pore pressure and stress effects from the full
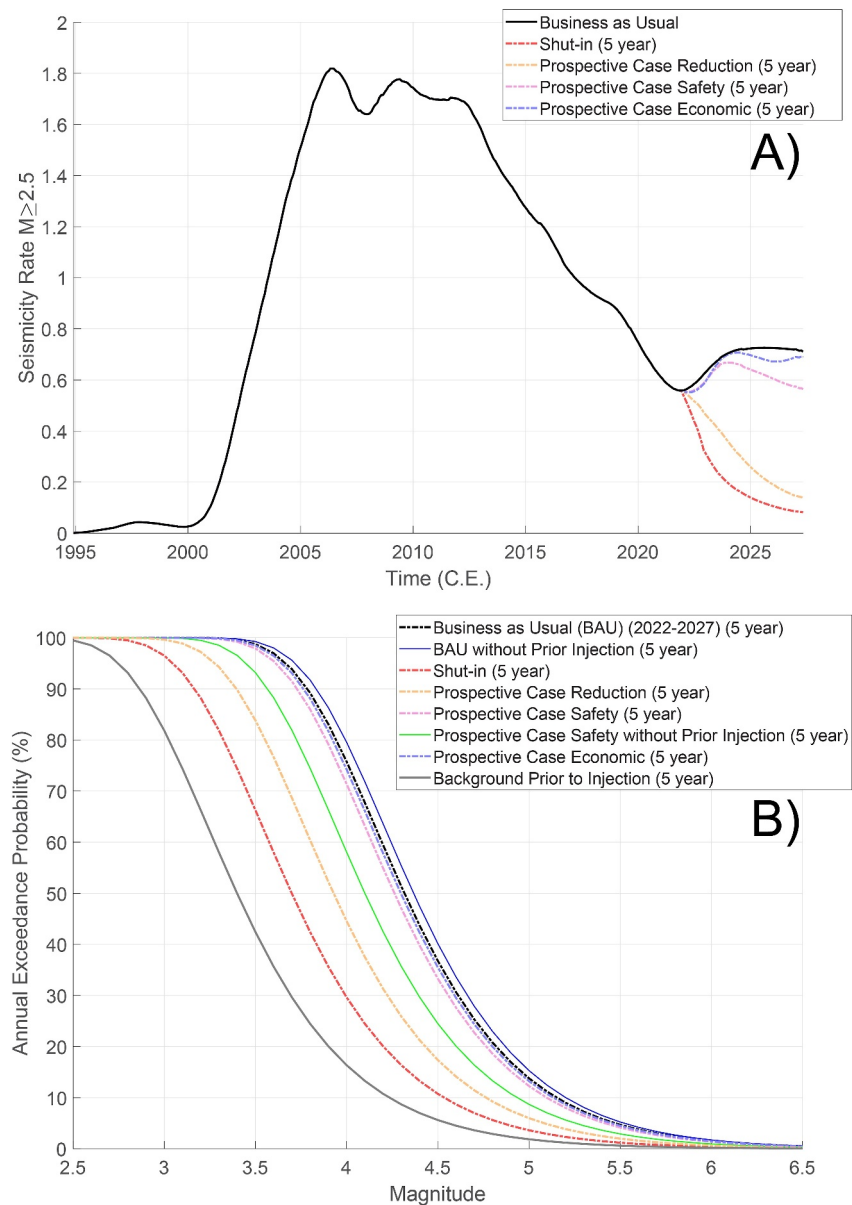
Figure 9. Seismicity Rate Forecasts and Forecasted Magnitude Exceedance Probabilities (Optimizations). (a) Seismicity rate for M≥2.5 from beginning of injection until beginning of optimization management period. Each of the 5 years optimizations have an associated exceedance probability in the next panel. (b) Exceedance probabilities for scenarios projected into the future (see main text). The Business as Usual (BAU) forecast is determined by extrapolating the last observed injection well data into the next 5 years. The shut-in forecast is determined in a similar way, but for immediate shut-in of all wells in June-2022. Prospective Case 'Reduction' considers reducing overall injection volume by 80% while not allowing the probability of exceeding a M≥4+ to be over 45%. Prospective case 'Safety' considers the same amount of fluid as the BAU case, but a more spatially optimized strategy based on the SI map. Prospective case 'Economic' optimizes to a solution for much more fluid for the same earthquake potential as the BAU case.

injection history (i.e., blue line in Figure 8). The 5 years earthquake potential for the shut-in scenario is also characterized spatially for a probability of exceeding a M≥4+ (Figure 11). Given enough prior seismicity to produce a SI map and a physical model to produce Coulomb stress rate any future injection scenarios can be considered in our model. We elaborate on three management models in the following sections.
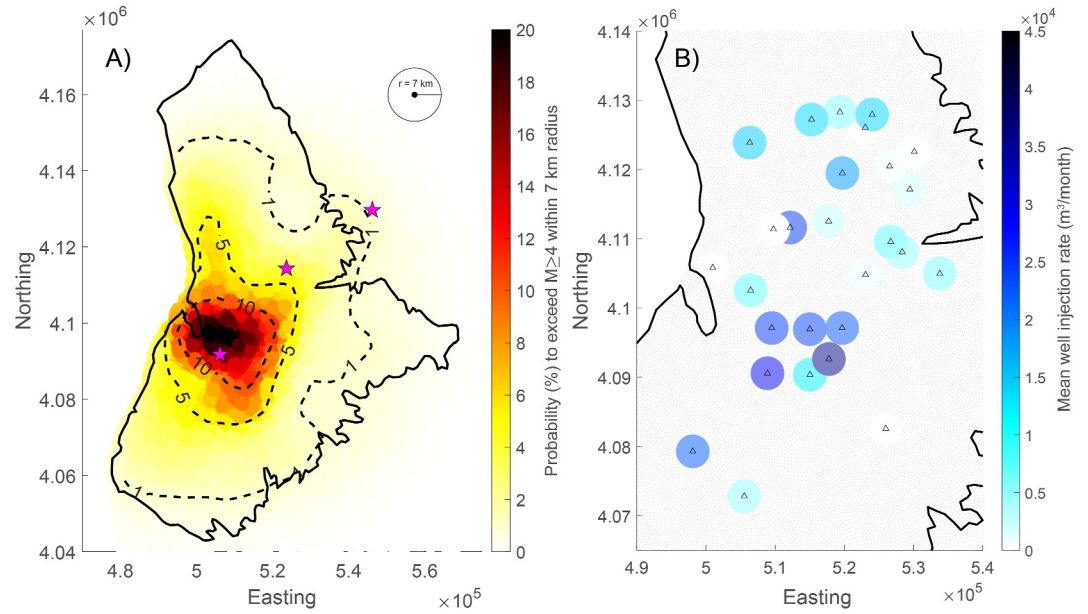
Figure 10. BAU Earthquake Potential and Mean Injection Rate. (a) Magnitude exceedance hazard map for M≥4+ for the 5 years management window. Each location is taken as the sum in a 7 km radius. Magenta stars (3) represent the locations of actually observed M≥4+ earthquakes between June-2022 and Sept-2023. (b) The Mean well injection rate (m^3/month) for all 29 wells (triangles) in the BAU extrapolation. Gray dots represent model nodes.

3. Physics-Based Forecasting With Optimization

3.1. Methods

The previous sections describe the methods to construct the simulation model built from two data sets: (a) the physics-based poroelastic model and (b) the statistical seismicity model or SI map (Figure 12). In this section we describe the additional methods required to frame our problem as a management model that allows for varied optimizations. In our optimization model, the objective function allows for the maximization of a desired objective, that is, total injection rate, using decision variables (monthly injection rates) subject to constraints, such as CFS rate at a particular location. In order to solve this optimization problem, we must build a response matrix of the system and use mixed-integer and linear programming to resolve our objective. An overview of the simulation-optimization procedure, including the construction of the simulation model, is provided in Figure 12.

3.1.1. Objective Function

In our study of the Raton Basin, the objective function is framed to maximize a desired objective over the 5-year management period. This objective function is maximized subjected to specific constraints, that is, Coulomb stress or Coulomb stress rate $\dot{\tau}$, below a threshold at chosen locations. Linear programming employs the unit-source solutions of the response matrix by linear superposition to acquire the optimal injection rates at each of the 29 wells in our model. The general framework of the linear program is represented as:

$$\min_q f^T q \tag{7}$$

subject to.

$$Rq \leq x \tag{8}$$

$$0 \leq q \leq ub \tag{9}$$

where q is the injection rate at each of the wells for each time step (i.e., monthly), f^T is a row vector of negative ones $[-1, \cdots, -1]$ so that the objective function seeks to maximize the cumulative injection, R is the response
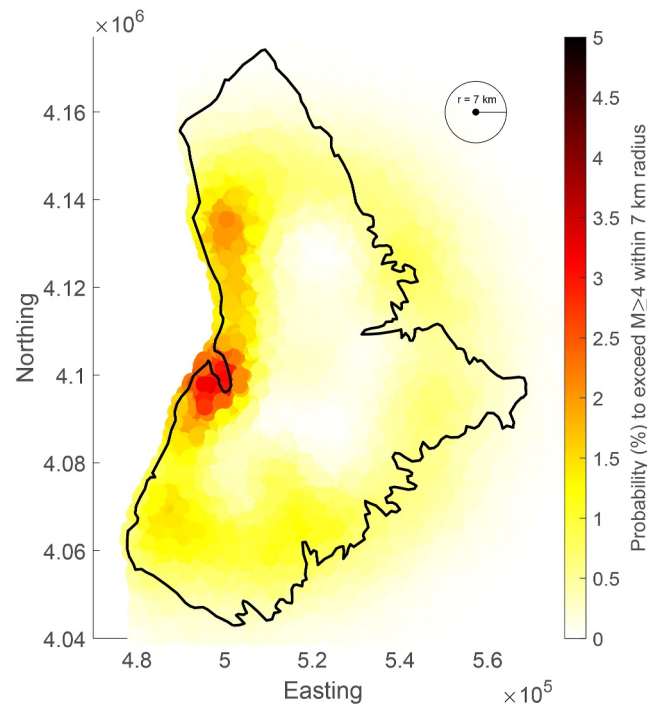
Figure 11. Shutin Earthquake Potential. The 5 years hazard for the shut-in scenario (all wells cease injection in May 2022 and stay off for 5 years) is also characterized spatially for a probability of exceeding a M≥4+. Shut-in represents the post-diffusion pore pressure and stress effects from the full injection history that continue to linger through the model and contribute to perturbations. Note that the colorbar axis is lower (5%) compared to all other maps which use 20% to clearly show the spatial distribution of the earthquake potential.

matrix (see Section 3.1.2), x is the constraint vector $\left(\dot{\tau}\right)$ at each of the model output locations, and ub is the upper bound on the monthly injection rate for each well. For all optimization scenarios presented, the upper bound for a single well injection rate is 1,500 m³/day, which represents the threshold of high-rate well injection nationwide (Weingarten et al., 2015). We solve the linear program using the linprog () function in MATLAB which generates optimal values of q, that is, the injection rates, for each well that do not exceed the constraints at the model output points. This objective function, subject to various constraints, is flexible and adaptable to a wide variety of adjustments within linear programming optimization. In Section 3.1.4, we elaborate on different ways to alter the management model constraints and provide a selection of controls that may be of interest to real-world injection practices.

3.1.2. Response Matrix

Given any linear system used to describe a given simulation model, a management model can be built with a response matrix. Construction of the response matrix requires individual unit-source solutions for each well operating within the management model. A unit-source solution is generated by producing an impulse from an individual well (i.e., unit flow rate) and measuring its response at all model output locations for the duration of the management period. The impulse has a fixed value for a specified period and a value of zero thereafter. The response of the system are changes in pore pressure and stress. Due to the linearity of the Coulomb stress equation (Equation 3), Coulomb stress and Coulomb stress rate are derived from this response (see Appendix for rate response matrix construction).

In our model, the Raton Basin contains 29 wells. Therefore, we must generate 29 independent, unit-source impulses (one for each well) and record the unit response at all model output locations. We must record each response for the entire 5-year management period (i.e., June-2022 to June-2027). Each time step in the model is 30 days. Hence, the unit-source response is a single flow rate equivalent to 100 m³/day for the first time step and then zero for the 60 months after. The result of this procedure is the unit-source response matrix of CFS rate
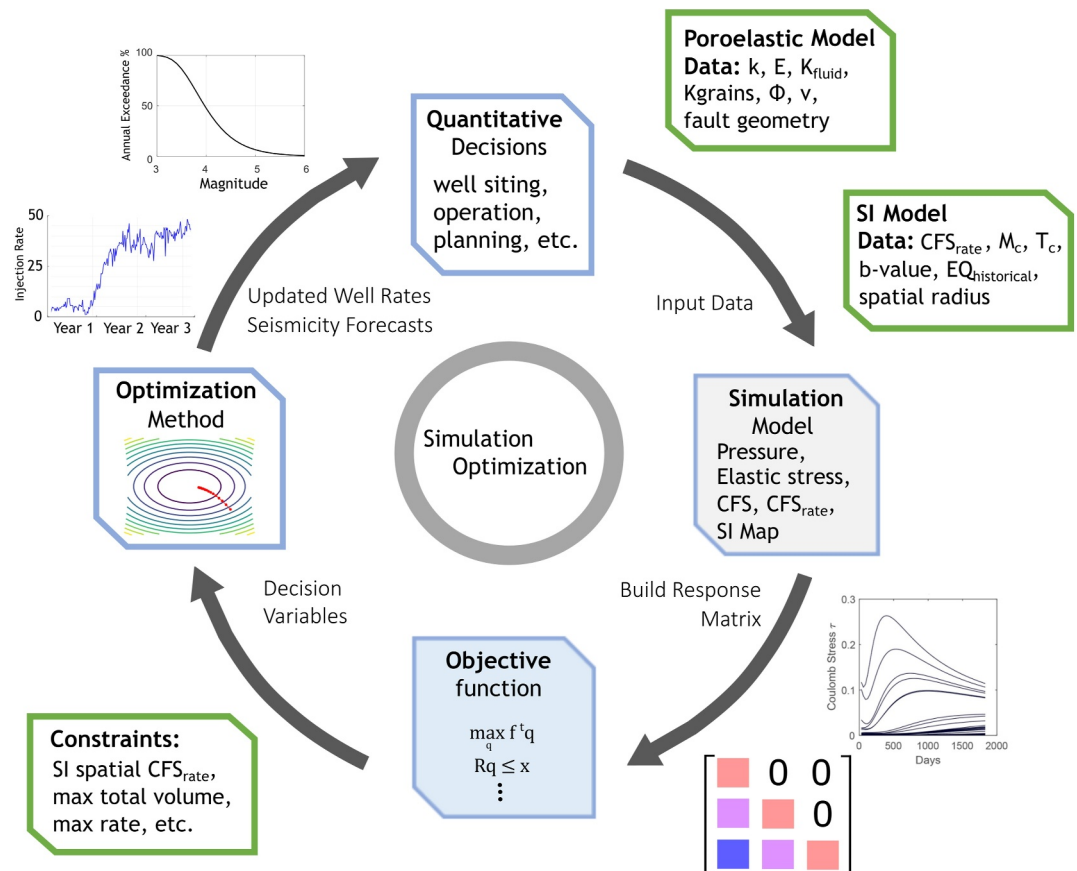
Figure 12. Simulation Optimization Schematic. Beginning at the top, operations consider quantitative decisions in well placing and operation prior to injection. By developing a numerical model and SI map from current injection a simulation model is built. The simulation model is used to build a response matrix which through linear programming solves a desired objective function (maximize the fluid injected). Additional constraints further inform the optimization which arrives at informed injection rates and spatial earthquake probability maps to then advise future operation practices.

produced by each well at every model output location (SM Figure 12 in Supporting Information S1). An example of this procedure is provided in the supplement (SM Methods 7.3 in Supporting Information S1; SM Figure 13 in Supporting Information S1).

3.1.3. Considering Injection Prior to Management Time Period

Our optimization management model optimizes injection rates under a set of given constraints for a prescribed management time period. It does not, inherently, consider injection prior to the management time period. We solve this issue by taking the difference of Coulomb stress between two simulations: (a) an ABAQUS simulation which considers all injection from Nov 1994 - 2027 (BAU rates) and (b) a response matrix simulation which considers only injection from 2022 to 2027 (BAU rates). The resulting Coulomb stressing rates represent the contribution of all prior injection during the management time period. This could be considered a 'complete shut-in' scenario from 2022 to 2027.

We calculated seismicity rates and a probability of exceedance curve expected from this shut-in scenario (Figure 9). Figure 11 depicts the spatial distribution of earthquake potential for yearly time steps. If wells were to have suddenly shut-in all wells in May 2022 our model predicts that there would still be a ~35% probability of exceeding a M>4+ earthquake in the next 5 years. The shut-in Coulomb stress rate perturbations are added to the Coulomb stress rate constraints of the optimization results prior to the seismicity rate and earthquake potential calculations, thus serving as the initial conditions or starting point in the optimizations. This step is essential, otherwise the earthquake potential is underestimated by the optimizations alone.

3.1.4. Mixed Integer Programming

Mixed-integer programming (MIP) allows the optimization manager to impose constraints that simulate real-world injection practices (Gorelick & Remson, 1982; Hsu & Yeh, 1989). Without MIP, the optimization solution is free to produce large swings in injection rate at individual wells. In reality, large injection wells have tolerances for injection rate changes over time. MIP allows the optimization manager to place controls what wells are operating and how the wells operate (independent or dependent on one another) through time. Injection rates can be constrained within a running average of past injection at a particular well, or monotonically increase or decrease injection through time, or exclude certain wells during certain periods.

The process of applying different types of MIP constraints is similar for most scenarios. First, a mixed-integer matrix is constructed R^* such that $R^*q \leq x^*$, where q is the corresponding injection well location for each management period and x^* is a vector of additional constraints. Both R^* and x^* are concatenated with original response matrix equation, Equation 8, and the objective function is maximized subject to these combined constraints (R and R^*). A simplified example is provided in SM Section 3, and further description of applying each type of MIP constraint in the management model is provided in SM Section 4.

3.1.5. Setting a Desired Earthquake Potential

The optimization problem described above is setup to constrain only CFS rate at specified locations through time. However, the optimization manager may still use our methodology to achieve a desired earthquake potential. This is performed by combining the calculated CFS rates with the SI model to produce seismicity rate forecasts. Optimization is still possible without coupling to a SI map if desired (See SM Section 3; SM Figure 16–17 in Supporting Information S1).

For a desired magnitude exceedance probability Pr(M) (Equation 6), a user can solve for the total number of earthquakes expected during the management period ($N_{\geq M}$). This $N_{\geq M}$, in combination with spatially varying SI map $\Sigma_\tau(r)$, can be used to calculate desired Coulomb stress rate constraints $x_{\dot{\tau}}$ for the management model:

$$x_{\dot{\tau}} = \frac{\partial}{\partial t}\tau_\tau(\boldsymbol{r}, t) = \sqrt{\frac{N_{\geq M}}{P \cdot T}10^{-\Sigma_\tau(r)+bM}} \tag{10}$$

where P now refers to the total number of constraint points in the SI model and T refers to the to total time chosen for the management period. This initialization assumes that each point in the model will carry a scaled portion of the total earthquake probability-that is, $\frac{N_{\geq M}}{P \cdot T}10^{bM}$ which is scaled by the SI (i.e., $10^{-\Sigma_\tau(r)}$). In our case, the total number of model points exceeds the computational limitation of the linear program and a subset of the total model points must be chosen. For example, the output of our model contains >30,000 points across the basin, but we reduce this total to 500 constraint locations for the management model. The chosen points are based on a uniform random distribution of points within a circle that contains all of the seismicity (SM Figure 18 in Supporting Information S1).

In practice, we have found that the CFS rate constraints provided by Equation 10 always produce a basin-wide Pr(M) lower than the desired threshold Pr(M). The desired threshold Pr(M) would only be met if the CFS rate constraint threshold is met at all points P for all time T. To resolve this issue, we iteratively solve the optimization model while increasing the CFS rate constraints at locations within the model that reached that threshold at any time during the management period. In this way, the constraints slowly increase based on which locations require a higher CFS rate in order to produce the desired Pr(M) in the basin. For our study, we set a goal of achieving the desired Pr(M) in the basin to within ±0.2% (see SM Section 5).

The following steps describe the methodology, generalized for application to other studies.

1. Choose a desired exceedance probability for an arbitrary magnitude threshold and solve for $N_{\geq M}$ (Equation 6).
2. Calculate CFS rate constraints for the management model (Equation 10).
3. Find optimal injection rates for calculated CFS rate constraints.
4. Calculate exceedance probabilities Pr(M) across the basin for the optimized solution.
5. Check if exceedance probabilities Pr(M) are within ±0.2% of desired Pr(M).
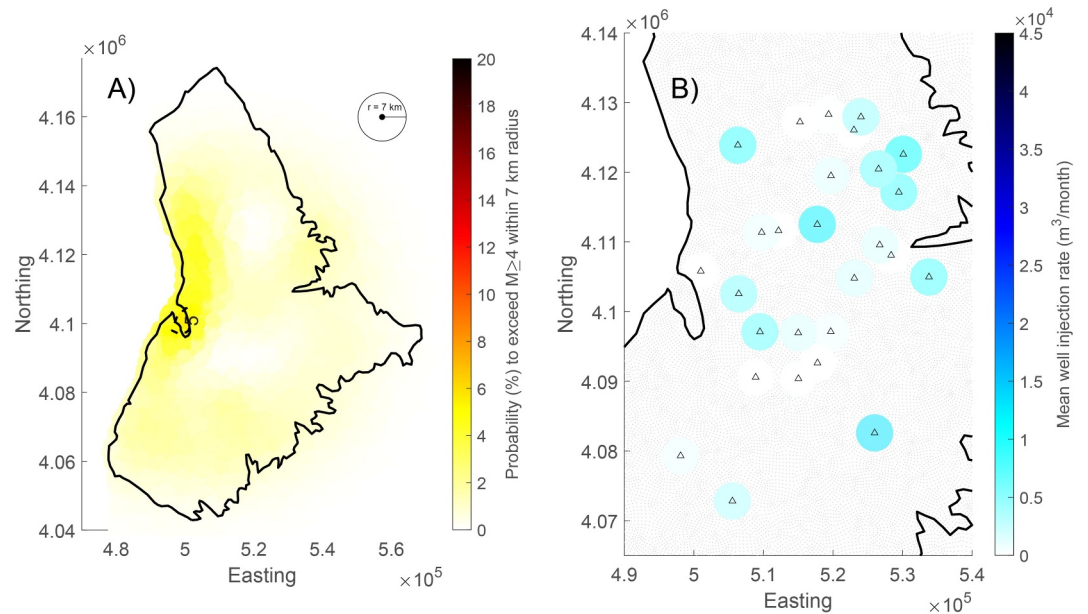6. If yes, skip steps 7 and 8.

Figure 13. Prospective Case 'Reduction' Results. (a) Magnitude exceedance earthquake potential map for M≥4+ for the 5 years management window. Each location is taken as the sum in a 7 km radius. See SM Figure 1 in Supporting Information S1 for yearly plots. (b) Mean injection rate (m³/month) at each well location (triangles). There are several locations where the optimization chooses not to inject. The gray dots represent the model nodes.

7. If no, adjust CFS rate constraints dependent on too high or too low of threshold.
8. Return to step 3.

3.2. Prospective Case 'Reduction' - Reduce the Earthquake Potential

The first prospective case we consider is called 'Reduction' (Figure 8 - Prospective Case Reduction). Prospective case 'Reduction' is the management solution for a hypothetical well operation that seeks to reduce the overall injection and maintain the earthquake potential within a chosen threshold. We include a constraint that the overall injection must be reduced by at least 80% from May 2022 levels by the end of the 5 years management window. Additionally, we constrained earthquake potential such that the probability of exceeding a M≥4+ event is 40% lower than the BAU forecast (Figure 9). The optimization and iterative method arrive at a solution to these constraints while maximizing the amount of fluid injected.

In order to achieve a smooth tapering of injection from the BAU initial injection rate of ~10,000 m³ per day we incorporate a MIP constraint to the management model. The constraint is a monotonic decrease of at least 2% each month for all injection wells (see SM Section 4) (Figure 8 - yellow line). This constraint smoothly reduces the overall injection rate and therefore the Coulomb stress rate by the end of the 5 year management period.

We find that there are several wells in the optimization that are never injecting, and that the algorithm preferentially chooses injectors toward the northeast more than other locations (Figure 13b). The northeast portion of the basin is a relatively low SI area (Figure 4). The west-central portion of the basin, which contains the highest SI hazard, does not have large amounts of injection during the management period. The optimization preferentially chooses to spread out large injectors from one another and to regions of lower SI (Figure 13b).

Another important observation is that prior injection still drives significant earthquake potential due to the time delay of pressure diffusion continuing to elevate the Coulomb stress rate in the periphery of the basin (Figure 13a). Earthquake potential is elevated in the west-central and western portion of the basin by prior injection, despite the optimization lowering injection in these areas. Our iterative technique still slowly reduces injection at wells and areas associated with high prior hazard if hazard thresholds are not initially met. In this way, our method takes into account prior injection through iterative forward solutions without direct inclusion in the optimization constraint vector (see SM Section 5).
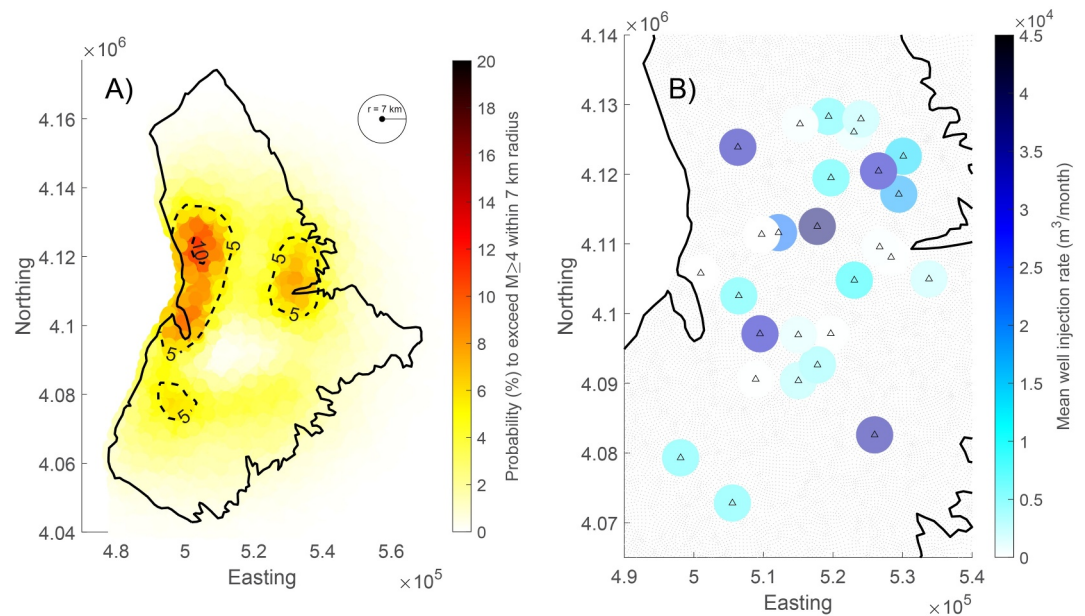
Figure 14. Prospective Case 'Safety' Results. (a) Total probability of exceeding a M≥4+ earthquake across the entire basin during the total 5 years management window. Earthquake potential is spread more evenly throughout the model and in less than the BAU case in areas that contribute to high hazard. See SM Figure 2 in Supporting Information S1 for yearly plots. (b) Mean injection rate in m^3/month at each well location (triangles). There are several locations where the optimization chooses not to inject. The gray dots represent the model nodes.

The enhanced hazard to the west in all of our models does not consider previously mapped faults unless they were captured by the SI map. This earthquake potential is primarily driven by continued Coulomb stress rate increase from prior injection. The inclusion of known faults is currently a limitation to our method. However, additional spatial constraints from known faults could be implemented as additional rows/elements in the response matrix/ constraint vector prior to optimization. Constraint thresholds of Coulomb stress or Coulomb stress rate could be applied to these known faults.

Visualizing the optimization at each time step is informative to the evolution of earthquake potential and how each individual well injects over time (SM Video 1 in Supporting Information S1). For the prospective case 'Reduction', wells inject continuously in the northeast - a low SI area - for the entire management period. Higher SI areas still receive injection but the optimization tends to spread the overall earthquake potential across the basin.

3.3. Prospective Case 'Safety'

Our second prospective case consider how the optimization algorithm might disperse BAU injection rates in order to minimize earthquake potential (i.e., 'Safety') (see Section 2.5 and Figure 8).

The second optimization solution, which we call prospective case 'Safety', seeks an optimized solution that lowers the overall earthquake potential while the basin-wide injection rate is constrained at May 2022 levels for the 5 years management period. The optimization will preferentially increase volume in wells where SI is lower, because the Coulomb stress rate constraints will be relaxed in these areas (see Equation 10). By moving injection volume to wells and areas with lower SI, the forecasted earthquake potential is reduced. The solution therefore produces an overall annual exceedance curve that is lower for the same total injection volume (Figure 8 - pink line).

Figure 14 describes the optimization results across the basin for prospective case 'Safety'. When the spatial distribution of injection is compared to the Business As Usual case, we find that the optimization spread injection volume out more evenly throughout the basin, instead of clustering injection in the central region. At the same, earthquake potential increases on the peripheries of basin away from the higher SI zones in the central basin. In the central basin, forecasted earthquake probability is reduced greatly, with less than 2% probability to exceed an
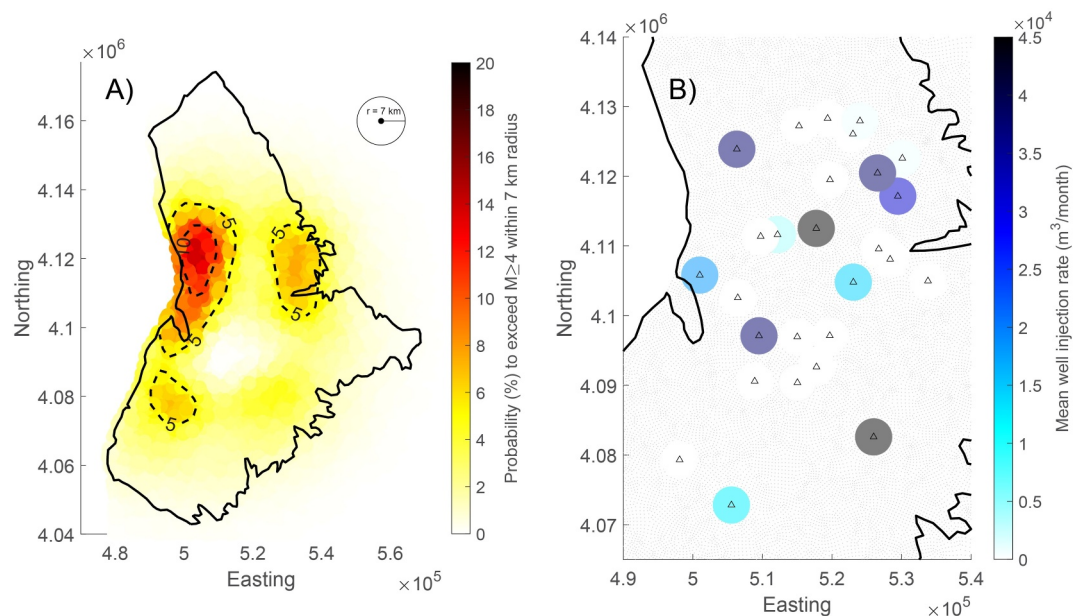
Figure 15. Prospective Case 'Economic' Results. (a) Total probability of exceeding a M≥4+ earthquake across the entire basin during the total 5 years management window. The highest probability western part of the basin is associated with the large fluid injection. See SM Figure 3 in Supporting Information S1 for yearly plots. (b) Mean injection rate in m^3/month at each well location (triangles). There are several locations where the optimization chooses not to inject. The gray dots represent the model nodes.

M≥4+ within 7 km. This is compared to nearly 20% probability to exceed an M≥4+ within 7 km in the Business As Usual case in the central basin. Forecasted earthquake potential is highest in the northeast portion of the basin, with 10% probability to exceed an M≥4+ within 7 km.

Our solution, during the 5 years management window, reduces the basin-wide annual exceedance probability M≥4+ from 75% to 71%. This optimized result is a relatively small reduction in the annual exceedance probabilities. However, we found that injection prior to the management period contributes to a large portion of the overall earthquake potential observed during the 5 years window. If the prospective case 'Safety' is run without prior injection, the optimization can reduce the annual exceedance probability M≥4+ from 75% to 58% (Figure 9 - green line). This reduction in earthquake potential is due to the optimization shifting injection to areas of lower SI.

Simply excluding prior injection does not, in and of itself, reduce the overall exceedance probabilities. We ran a earthquake potential forecast for the Business As Usual case excluding prior injection and found the annual exceedance probability for a M≥4+ earthquake increased from 75% to 80% (Figure 9 - BAU without prior injection line). The reason for this increase in overall earthquake potential when excluding prior injection is that prior injection was on a long-term decline, especially in areas with high SI. These declining injection rates prior to the management time period actually reduce the Coulomb stress rate in areas where the BAU injection is high. Therefore, counter intuitively, excluding prior injection increases the earthquake potential in the BAU case and decreases in the 'Safety' case.

The results from the 'Safety' case reveal that prior injection can have a large influence on how much the optimization method reduces overall earthquake potential. Furthermore, it highlights the importance of optimizing injection as early as possible in the course of an induced seismic sequence. In the case of Raton Basin, injection and induced seismicity have been ongoing for multiple decades, which reduce the positive safety effects of minimizing earthquake potential during the management period.

3.4. Prospective Case 'Economic'

The third optimization solution, which we call prospective case 'Economic', seeks to increase the overall injection rate but maintain the same basin-wide earthquake potential as the BAU case (see Section 2.5 and Figure 8).

In this case, we allow the optimization freedom to increase the overall volume that can be injected in any month of the 5 years management window. An optimal solution is found when the basin-wide annual exceedance probabilities are within ≤2% of the BAU probability of exceedance for M≥4+ (∼75%). We include two constraints on individual wells in this solution: (a) no individual well injection rate can exceed 1,500 m^3/day, and (b) an MIP constraint that limits individual well injection rates to within a 6-month running average so that the optimization cannot drastically front-load or back-load the management period with injection volume. Again, the Coulomb stress rate constraints derived from the SI map force the optimization to preferentially increase volume in areas away from the largest earthquake potential (i.e., lower SI).

An optimal solution was found for the 'Economic' case, which increased the overall injection rate basin-wide compared to the BAU case (Figure 8 - green line). The solution shows a gradual increase in basin-wide injection rate from ∼300,000 m³/month in 2022 to ∼375,000 m³/month in 2027. The increase in cumulative volume injected in the 'Economic' case is more than 1,080,000 m^3 (∼6,750,000 barrels) when compared to the BAU case.

The spatial distribution of injection in the 'Economic' case shows a substantial change in the how the field would be operated during the 5 years management period (Figure 15b). Of the 29 potential injection wells, the optimization chooses to inject at only 12 wells, while the remaining 17 are completely shut-in. Of the 12 wells which operate during the 5 years window, only 6 inject at rates higher than 20,000 m³/month. These six injectors, where the vast majority of fluid is injected, are spread out across the entirety of the well field and to regions of lower SI. These 6 wells inject at a more or less a constant rate for the entire management time (SM Video three in Supporting Information S1). Clustering of injection is held to a minimum when compared to the 'Reduction' or 'Safety' case.

This case highlights what the optimization method ultimately attempts to achieve: spatially distributed injection across regions of lower SI. By spreading out injectors, the basin-wide Coulomb stress rate is reduced by minimizing superposition of clustered injectors. By concentrating injection in regions of lower SI, the Coulomb stress rate that is created by injection results in lower induced seismicity. This combination of effects—spatially distributed injection in regions of lower SI—allows for the highest basin-wide injection rates (and largest cumulative injected volume) for a given earthquake potential.

4. Discussion

The combination of physics-based forecasting with optimization management shows promise for future work in mitigating induced earthquake potential at the basin-scale. The optimization framework allows a user to maximize a particular objective (i.e., reduction, safety, or economic) while maintaining a specified induced earthquake potential. Our method is also flexible and adaptable to other regions or other types of fluid injection that induce seismicity. The main components are the following.

1. **Physics-based model of pressure and/or stress change**. First, a physics-based model of injection must be built of the region that has good estimates of the relevant reservoir flow parameters. Here, we have built a fully coupled, poroelastic numerical model using the finite-element method calibrated using injection data from reservoir step-rate tests. However, a finite-difference model could also work (e.g., MODFLOW). Any linear system is the key. Depending on whether the poroelastic stress effects are marginal to the pore pressure effects may influence this decision.
2. **Seismogenic Index (SI) Map.** Second, a SI map (see Section 2.3) must be calibrated from the empirical relationship of seismic response to injection. Thus, some degree of prior injection and earthquake history are required for forecasting. Without the SI map, optimization is still possible, but will not be constrained by a desired earthquake potential.
3. **Response Matrix.** Third, a response matrix of the system is built from impulse-responses of the system to a unit injection at each prospective injection site (see Section 3.1.2). The response matrix allows the optimization to scale injection rates of individual wells to find the combination which satisfies the constraints and maximizes the objective function.
4. **Optimization Framework.** Lastly, an optimization framework of an objective function, constraints, and decision variables are input. The model then seeks the optimized solution that will satisfy either a reduction, safety or economic objective and maximize fluid injected.

The adaptability of this method to other regions is possible through the gathering of required basin-specific input data on reservoir flow parameters, injection and seismicity response. In addition, the method is flexible enough to consider any fluid injection that produces a linear poroelastic response. Listed below are some of the potential improvements and limitations of the current framework.

1. **Real-time optimization and forecasting:** Once the physics-based model and SI map are initially calibrated the user could develop an optimal injection strategy and continuously update the SI map if seismicity evolves in new areas. The response matrix method allows for quick integration of new constraints without the need to re-run elaborate physical models continuously. Therefore, rapid adjustments in well optimization are possible as the SI adjusts and improves in new areas of the basin.

2. **Stacked optimization for model uncertainty:** As described in SM Section 4, stacked optimization allows the user to find one set of optimal injection rates that explicitly account for the uncertainty in the physical model. The existing framework contains uncertainty in the earthquake potential due to the Poisson distribution within the SI model. However, stacked optimization allows the user to consider uncertainty within the physical model (i.e., a distribution of flow parameters). Stacked optimization does require more computational power as it requires N (where N is the number of wells) additional model runs for each uncertain distribution to be appended to the response matrix.

3. **Non-linear programming:** Non-linear programming allows optimization of non-linear objective functions and constraints. Currently, our linear program cannot explicitly optimize injection using earthquake potential (R) as a constraint because R is non-linearly related to CFS rate. Therefore, we rely on an iterative approach to optimize injection to a desired earthquake potential (see SM Section 5). Non-linear programming may be able to address the issue of local-minima in the optimal solution where currently non-unique solutions may be found by a linear program. Our iterative method slowly adjusts the constraint locations one at a time to prevent any over saturation in earthquake potential and injected fluid at any one location in the solution. Non-linear programming may be able to save computational time as compared to the iterative approach.

4. **Incorporating known fault maps:** A key piece of future work is the integration of known fault maps within the optimization framework. Known faults would serve as additional constraint locations appended to the response matrix and constraint vector, where pressure and/or stress change would be limited. From a practical point of view, known faults in many cases of induced seismicity are not the primary drivers of induced earthquake potential (i.e., Oklahoma), but users may desire to avoid stressing faults when optimizing basin-scale injection. This optimization framework would allow the consideration of both an SI map and fault maps.

5. **Incorporating risk for policy:** While we looked at the total earthquake potential in the region, it would be possible to constrain hazard spatially depending on seismic risk (Schultz et al., 2021). For example, agreement might be met with industrial well operations that maximizes the fluid injected while restricting earthquake potential in an area with high risk, like a densely populated area. A scientifically informed policy, for example, one that limits the probability of exceeding a M≥5+ earthquake within a high risk zone, could be met while still reaching the economic objective of the well operators.

5. Conclusions

Here, we investigated the relationship between wastewater injection and seismicity in the Raton Basin of Colorado and New Mexico using a physics-based forecasting framework. First, a 3D finite element model of a poroelastic crust is used to estimate time dependent Coulomb stress changes over the more than two decades of Raton Basin injection. The outputs of Coulomb stress rate from our finite element model were combined with a seismogenic index (SI) model to forecast induced seismicity in space and time throughout the basin. Using this hybrid physics-statistical forecasting model we found the following conclusions.

1. The recent and ongoing induced seismicity within the Raton Basin is well explained by our physics-based forecasting model. Declining seismicity rates between 2016 and 2022 are forecasted well by the decline in basin-wide injection rate. Despite injection rate declines, modeled Coulomb stress rate is still increasing in several regions of the basin, suggesting that induced earthquake potential is still ongoing. Our model also shows that induced seismicity is driven primarily by the pore pressure component of the poroelastic stresses, with poroelastic stress changes accounting for about 5% of the driving force.

2. Using our physics-based forecasting model, we estimated the induced earthquake potential produced by continued Raton Basin injection at May 2022 levels through 2027 (Business As Usual case). Our 5 years forecast estimates the probability to exceed a M≥4+ event is 75% and M≥5+ event 14%.

3. Linear-programming optimization using the response matrix method is implemented successfully using a safety objective framework that reduces earthquake potential for a given amount of fluid injection (safety objective) or (b) maximizes fluid injection for a prescribed earthquake potential (economic objective).

4. Across the different objectives tested, the optimization algorithm tends to spread injection out across the field when compared to the Business As Usual case. In the safety and economic objective cases, we observed the algorithm spreading out higher rate injection wells from one another and to regions of lower seismogenic index (SI). We also demonstrate that injection prior to the optimization management period may have differing effects on earthquake potential during the management period. In the reduction and safety cases, we show that prior injection enhanced earthquake potential during the management period, thus decreasing the impact of injection optimization. We conclude that optimization of injection earlier in an induced sequence will allow for better control of earthquake potential during the management period.

Appendix A: Coulomb Stress Rate Response Matrix

The *rate* response matrix is represented as differences in the original Response Matrix between adjacent time intervals, analogous to a derivative. It is helpful to define components of the original Response Matrix as $R_{n,w,t}$ corresponding to the response at n model output points by w wells during the time interval t. Similarly, the injection rate for all wells w during the time interval t is given by $q_{w,t}$ One of these components is equivalent to the colored blocks in SM Figure 12 in Supporting Information S1.

It is informative to expand on the derivation of the *rate* response matrix by working out how each time step portion is generated, and its relation to the rate constraint. First, the initial time step is simply:

$$R_{n,w,1}q_{w,1} \leq \dot{x}_{n,1}$$

Then for the second time step, rate constraint $x_{n,2}$ must satisfy the difference between the response generated in step 2 from the response generated prior. In other words, the difference between the second 'row' of the Response Matrix (the response at $t = 1$) and the response at $t = 2$:

$$\left(R_{n,w,2}q_{w,1} + R_{n,w,1}q_{w,2}\right) - \left(R_{n,w,1}q_{w,1}\right) \leq \dot{x}_{n,2}$$

Which, we then factor out the independent injection rates at specific time steps from:

$$\left(R_{n,w,2} - R_{n,w,1}\right)q_{w,1} + \left(R_{n,w,1}\right)q_{w,2} \leq \dot{x}_{n,2}$$

Repeating the two steps above for the next time step, a pattern begins to emerge:

$$\left(R_{n,w,3}q_{w,1} + R_{n,w,2}q_{w,2} + R_{n,w,1}q_{w,3}\right) - \left(R_{n,w,2}q_{w,1} + R_{n,w,1}q_{w,2}\right)$$
$$\leq \dot{x}_{n,3}\left(R_{n,w,3} - R_{n,w,2}\right)q_{w,1} + \left(R_{n,w,2} - R_{n,w,1}\right)q_{w,2} + \left(R_{n,w,1}\right)q_{w,3} \leq \dot{x}_{n,3}$$

so that in general the rows for each time step t of the *rate* response matrix $\dot{R}_{n,w,t}$ are appended by:

$$\dot{R}_{n,w,t} = \sum_{N=0}^{t-1}(R_{n,w,t-N} - R_{n,w,t-N-1})$$

Therefore, the coefficients for each $q_{w,t}$ factor can be combined in a *rate* response matrix which only requires the individual $R_{n,w,t}$ components from the original response matrix to generate. Once generated, if desired, you can choose to optimize the injection rate from the rate constraints exclusively or combined with other constraints.

Data Availability Statement

The wastewater injection data is available from the Colorado Oil and Gas Corporation Commission website (COGCC, 2024, https://ecmc.state.co.us/data.html#/cogis). The wastewater injection data is available from the

New Mexico Oil Conservation Division Permitting website (NMOCD, 2024, https://wwwapps.emnrd.nm.gov/OCD/OCDPermitting/Data/Wells.aspx). Data of Abaqus files, post-processing scripts, SI model scripts, optimization methodology scripts, and figure generation scripts are available online Hill (2024).

References

Bachmann, C. E., Wiemer, S., Goertz-Allmann, B., & Woessner, J. (2012). Influence of pore-pressure on the event-size distribution of induced earthquakes. *Geophysical Research Letters*, *39*(9). https://doi.org/10.1029/2012gl051480

Bao, X., & Eaton, D. W. (2016). Fault activation by hydraulic fracturing in western Canada. *Science*, *354*(6318), 1406–1409. https://doi.org/10.1126/science.aag2583

Barnhart, W. D., Benz, H. M., Hayes, G. P., Rubinstein, J. L., & Bergman, E. (2014). Seismological and geodetic constraints on the 2011 Mw5. 3 Trinidad, Colorado earthquake and induced deformation in the Raton Basin. *Journal of Geophysical Research: Solid Earth*, *119*(10), 7923–7933. https://doi.org/10.1002/2014jb011227

Belitz, K., & Bredehoeft, J. D. (1988). Hydrodynamics of Denver Basin: Explanation of subnormal fluid pressures. *AAPG Bulletin*, *72*(11), 1334–1359. https://doi.org/10.1306/703c999c-1707-11d7-8645000102c1865d

Biot, M. A. (1941). General theory of three-dimensional consolidation. *Journal of Applied Physics*, *12*(2), 155–164. https://doi.org/10.1063/1.1712886

Brace, W. F. (1980). Permeability of crystalline and argillaceous rocks. *International Journal of Rock Mechanics and Mining Sciences & Geomechanics Abstracts*, *17*(5), 241–251. https://doi.org/10.1016/0148-9062(80)90807-4

Cacace, M., Hofmann, H., & Shapiro, S. A. (2021). Projecting seismicity induced by complex alterations of underground stresses with applications to geothermal systems. *Scientific Reports*, *11*(1), 23560. https://doi.org/10.1038/s41598-021-02857-0

Caine, J. S., Evans, J. P., & Forster, C. B. (1996). Fault zone architecture and permeability structure. *Geology*, *24*(11), 1025–1028. https://doi.org/10.1130/0091-7613(1996)024<1025:fzaaps>2.3.co;2

Clark, K., Northrop, S., & Read, C. (1966). Geology of the Sangre de Cristo Mountains and adjacent areas, between Taos and Raton, New Mexico. In *Taos-Raton-Spanish peaks country (New Mexico and Colorado): Geological society 17th annual fall field conference guidebook* (pp. 56–65).

Cocco, M., & Rice, J. R. (2002). Pore pressure and poroelasticity effects in Coulomb stress analysis of earthquake interactions. *Journal of Geophysical Research*, *107*(B2), 2030. https://doi.org/10.1029/2000jb000138

COGCC. (2024). Colorado oil and gas corporation commission website. [Dataset] Retrieved from https://ecmc.state.co.us/data.html#/cogis. Accessed 10 10 2023.

Dassault Systemes. (2020). Abaqus (version 2019).

Detournay, E., & Cheng, A. H.-D. (1993). Fundamentals of poroelasticity. In *Analysis and design methods* (pp. 113–171). Elsevier.

Ellsworth, W. L. (2013). Injection-induced earthquakes. *Science*, *341*(6142). https://doi.org/10.1126/science.1225942

Fialko, Y. (2004). Evidence of fluid-filled upper crust from observations of post-seismic deformation due to the 1992 M_w7.3 Landers earthquake. *Journal of Geophysical Research*, *109*(B8), B08401. https://doi.org/10.1029/2004jb002985

Fialko, Y., & Simons, M. (2000). Deformation and seismicity in the Coso geothermal area, Inyo County, California: Observations and modeling using satellite radar interferometry. *Journal of Geophysical Research*, *105*(B9), 21781–21793. https://doi.org/10.1029/2000jb900169

Foulger, G. R., Wilson, M. P., Gluyas, J. G., Julian, B. R., & Davies, R. J. (2018). Global review of human-induced earthquakes. *Earth-Science Reviews*, *178*, 438–514. https://doi.org/10.1016/j.earscirev.2017.07.008

Ge, S., & Saar, M. O. (2022). Induced seismicity during geoenergy development—A hydromechanical perspective. *Journal of Geophysical Research: Solid Earth*, *127*(3), e2021JB023141. https://doi.org/10.1029/2021jb023141

Geldon, L. (1989). *Ground-water hydrology of the central Raton Basin*. Colorado and New Mexico.

Giardini, D. (2009). Geothermal quake risks must be faced. *Nature*, *462*(7275), 848–849. https://doi.org/10.1038/462848a

Glasgow, M., Schmandt, B., Wang, R., Zhang, M., Bilek, S., & Kiser, E. (2021a). Raton basin 2016-2020 earthquake catalog. *International Seismological Centre*. https://doi.org/10.31905/127xp53r

Glasgow, M., Schmandt, B., Wang, R., Zhang, M., Bilek, S. L., & Kiser, E. (2021b). Raton Basin induced seismicity is hosted by networks of short basement faults and mimics tectonic earthquake statistics. *Journal of Geophysical Research: Solid Earth*, *126*(11), e2021JB022839. https://doi.org/10.1029/2021jb022839

Goertz-Allmann, B. P., Kühn, D., Oye, V., Bohloli, B., & Aker, E. (2014). Combining microseismic and geomechanical observations to interpret storage integrity at the In Salah CCS site. *Geophysical Journal International*, *198*(1), 447–461. https://doi.org/10.1093/gji/ggu010

Gorelick, S. M. (1983). A review of distributed parameter groundwater management modeling methods. *Water Resources Research*, *19*(2), 305–319. https://doi.org/10.1029/wr019i002p00305

Gorelick, S. M., Freeze, R. A., Donohue, D., Keely, J. F., et al. (1993). *Groundwater contamination: Optimal capture and containment*. Lewis Publishers Inc.

Gorelick, S. M., & Remson, I. (1982). Optimal dynamic management of groundwater pollutant sources. *Water Resources Research*, *18*(1), 71–76. https://doi.org/10.1029/wr018i001p00071

Gorelick, S. M., & Zheng, C. (2015). Global change and the groundwater management challenge. *Water Resources Research*, *51*(5), 3031–3051. https://doi.org/10.1002/2014wr016825

Grasso, J.-R., & Wittlinger, G. (1990). Ten years of seismic monitoring over a gas field. *Bulletin of the Seismological Society of America*, *80*(2), 450–473.

Higley, D. K. (2007). *Petroleum systems and assessment of undiscovered oil and gas in the Raton Basin–sierra grande uplift province, Colorado and New Mexico—USGS province 41*. US Geological Survey. No. 69-N.

Hill, R. G. (2024). Data and code for modeling Raton Basin. *Zenodo*. [Dataset]. https://doi.org/10.5281/zenodo.10472485

Hill, R. G., Weingarten, M., Rockwell, T. K., & Fialko, Y. (2023). Major southern San Andreas earthquakes modulated by lake-filling events. *Nature*, *618*(7966), 761–766. https://doi.org/10.1038/s41586-023-06058-9

Hsu, N.-S., & Yeh, W. W.-G. (1989). Optimum experimental design for parameter identification in groundwater hydrology. *Water Resources Research*, *25*(5), 1025–1040. https://doi.org/10.1029/wr025i005p01025

Jin, L. (2023). On a saturated poromechanical framework and its relation to abaqus soil mechanics and biot poroelasticity frameworks. *arXiv Preprint arXiv:2304.02148*.

Jin, L., Curry, W. J., Lippoldt, R. C., Hussenoeder, S. A., & Bhargava, P. (2023). 3d coupled hydro-mechanical modeling of multi-decadal multi-zone saltwater disposal in layered and faulted poroelastic rocks and implications for seismicity: An example from the midland basin. *Tectonophysics*, *863*, 229996. https://doi.org/10.1016/j.tecto.2023.229996

Jin, Z., Fialko, Y., Zubovich, A., & Schöne, T. (2022). Lithospheric deformation due to the 2015 M7.2 Sarez (Pamir) earthquake constrained by 5 years of space geodetic observations. *Journal of Geophysical Research*, *127*(4), e2021JB022461. https://doi.org/10.1029/2021jb022461

Keranen, K. M., & Weingarten, M. (2018). Induced seismicity. *Annual Review of Earth and Planetary Sciences*, *46*(1), 149–174. https://doi.org/10.1146/annurev-earth-082517-010054

Keranen, K. M., Weingarten, M., Abers, G. A., Bekins, B. A., & Ge, S. (2014). Sharp increase in central Oklahoma seismicity since 2008 induced by massive wastewater injection. *Science*, *345*(6195), 448–451. https://doi.org/10.1126/science.1255802

Kettlety, T., Verdon, J. P., Werner, M. J., & Kendall, J. (2020). Stress transfer from opening hydraulic fractures controls the distribution of induced seismicity. *Journal of Geophysical Research: Solid Earth*, *125*(1), e2019JB018794. https://doi.org/10.1029/2019jb018794

King, G. C. P., Stein, R. C., & Lin, J. (1994). Static stress change and the triggering of earthquakes. *Bulletin of the Seismological Society of America*, *84*, 935–953.

LaBonte, A., Brown, K., & Fialko, Y. (2009). Hydrogeologic detection and finite-element modeling of a slow-slip event in the Costa Rica prism toe. *Journal of Geophysical Research*, *114*(B4), B00A02. https://doi.org/10.1029/2008jb005806

Langenbruch, C., Dinske, C., & Shapiro, S. (2011). Inter event times of fluid induced earthquakes suggest their Poisson nature. *Geophysical Research Letters*, *38*(21). https://doi.org/10.1029/2011gl049474

Langenbruch, C., Weingarten, M., & Zoback, M. D. (2018). Physics-based forecasting of man-made earthquake hazards in Oklahoma and Kansas. *Nature Communications*, *9*(1), 1–10. https://doi.org/10.1038/s41467-018-06167-4

Langenbruch, C., & Zoback, M. D. (2016). How will induced seismicity in Oklahoma respond to decreased saltwater injection rates? *Science Advances*, *2*(11), e1601542. https://doi.org/10.1126/sciadv.1601542

Macartney, H., & O'Farrell, C. (2010). *A Raton Basin geothermal prospect*. AAPG. CO.

Majer, E. L., & Peterson, J. E. (2007). The impact of injection on seismicity at the Geysers, California Geothermal Field. *International Journal of Rock Mechanics and Mining Sciences*, *44*(8), 1079–1090. https://doi.org/10.1016/j.ijrmms.2007.07.023

Mignan, A., Landtwing, D., Kästli, P., Mena, B., & Wiemer, S. (2015). Induced seismicity risk analysis of the 2006 Basel, Switzerland, Enhanced Geothermal System project: Influence of uncertainties on risk mitigation. *Geothermics*, *53*, 133–146. https://doi.org/10.1016/j.geothermics.2014.05.007

Moein, M. J., Langenbruch, C., Schultz, R., Grigoli, F., Ellsworth, W. L., Wang, R., et al. (2023). The physical mechanisms of induced earthquakes. *Nature Reviews Earth and Environment*, *4*(12), 847–863. https://doi.org/10.1038/s43017-023-00497-8

Nakai, J., Weingarten, M., Sheehan, A., Bilek, S., & Ge, S. (2017a). A possible causative mechanism of Raton Basin, New Mexico and Colorado earthquakes using recent seismicity patterns and pore pressure modeling. *Journal of Geophysical Research: Solid Earth*, *122*(10), 8051–8065. https://doi.org/10.1002/2017jb014415

Nelson, P. H., Gianoutsos, N. J., & Anna, L. O. (2013). *Outcrop control of basin-scale underpressure in the Raton Basin*. Colorado and New Mexico.

NMOCD. (2024). New Mexico oil conservation division permitting website. [Dataset] Retrieved from https://wwwapps.emnrd.nm.gov/OCD/OCDPermitting/Data/Wells.aspx. Accessed 10 10 20223.

Pearse, J., & Fialko, Y. (2010). Mechanics of active magmatic intraplating in the rio grande rift near socorro, New Mexico. *Journal of Geophysical Research*, *115*(B7), B07413. https://doi.org/10.1029/2009jb006592

Rice, J. R., & Cleary, M. P. (1976). Some basic stress diffusion solutions for fluid-saturated elastic porous media with compressible constituents. *Reviews of Geophysics*, *14*(2), 227–241. https://doi.org/10.1029/RG014i002p00227

Ross, Z. E., Cochran, E. S., Trugman, D. T., & Smith, J. D. (2020). 3d fault architecture controls the dynamism of earthquake swarms. *Science*, *368*(6497), 1357–1361. https://doi.org/10.1126/science.abb0779

Rubinstein, J. L., Ellsworth, W. L., McGarr, A., & Benz, H. M. (2014). The 2001–present induced earthquake sequence in the Raton Basin of northern New Mexico and southern Colorado. *Bulletin of the Seismological Society of America*, *104*(5), 2162–2181. https://doi.org/10.1785/0120140009

Rudnicki, J. W. (1986). Fluid mass sources and point forces in linear elastic diffusive solids. *Mechanics of Materials*, *5*(4), 383–393. https://doi.org/10.1016/0167-6636(86)90042-6

Rutqvist, J., Rinaldi, A. P., Cappa, F., & Moridis, G. J. (2015). Modeling of fault activation and seismicity by injection directly into a fault zone associated with hydraulic fracturing of shale-gas reservoirs. *Journal of Petroleum Science and Engineering*, *127*, 377–386. https://doi.org/10.1016/j.petrol.2015.01.019

Schultz, R., Beroza, G. C., & Ellsworth, W. L. (2021). A risk-based approach for managing hydraulic fracturing–induced seismicity. *Science*, *372*(6541), 504–507. https://doi.org/10.1126/science.abg5451

Segall, P. (2010). *Earthquake and volcano deformation*. Princeton University Press.

Segall, P., & Lu, S. (2015). Injection-induced seismicity: Poroelastic and earthquake nucleation effects. *Journal of Geophysical Research: Solid Earth*, *120*(7), 5082–5103. https://doi.org/10.1002/2015jb012060

Shapiro, S. A., Dinske, C., Langenbruch, C., & Wenzel, F. (2010). Seismogenic index and magnitude probability of earthquakes induced during reservoir fluid stimulations. *The Leading Edge*, *29*(3), 304–309. https://doi.org/10.1190/1.3353727

Shirzaei, M., Ellsworth, W. L., Tiampo, K. F., González, P. J., & Manga, M. (2016). Surface uplift and time-dependent earthquake potential due to fluid injection in eastern Texas. *Science*, *353*(6306), 1416–1419. https://doi.org/10.1126/science.aag0262

Shmonov, V., Vitiovtova, V., Zharikov, A., & Grafchikov, A. (2003). Permeability of the continental crust: Implications of experimental data. *Journal of Geochemical Exploration*, *78*, 697–699. https://doi.org/10.1016/s0375-6742(03)00129-8

Snee, J.-E. L., & Zoback, M. D. (2022). State of stress in areas of active unconventional oil and gas development in North America. *AAPG Bulletin*, *106*(2), 355–385. https://doi.org/10.1306/08102120151

Stokes, S. M., Ge, S., Brown, M. R., Menezes, E. A., Sheehan, A. F., & Tiampo, K. F. (2023). Pore pressure diffusion and onset of induced seismicity. *Journal of Geophysical Research: Solid Earth*, *128*(3), e2022JB026012. https://doi.org/10.1029/2022jb026012

Townend, J., & Zoback, M. D. (2000). How faulting keeps the crust strong. *Geology*, *28*(5), 399–402. https://doi.org/10.1130/0091-7613(2000)028<0399:hfktcs>2.3.co;2

van Thienen-Visser, K., & Breunese, J. (2015). Induced seismicity of the Groningen gas field: History and recent developments. *The Leading Edge*, *34*(6), 664–671. https://doi.org/10.1190/tle34060664.1

Walsh, F. R., III, & Zoback, M. D. (2015). Oklahoma's recent earthquakes and saltwater disposal. *Science Advances*, *1*(5), e1500195. https://doi.org/10.1126/sciadv.1500195

Wang, H. (2000). *Theory of linear poroelasticity: With applications to geomechanics and hydrogeology* (p. 287). Princeton University Press.

Wang, R., Schmandt, B., Zhang, M., Glasgow, M., Kiser, E., Rysanek, S., & Stairs, R. (2020). Injection-induced earthquakes on complex fault zones of the Raton Basin illuminated by machine-learning phase picker and dense nodal array. *Geophysical Research Letters*, *47*(14), e2020GL088168. https://doi.org/10.1029/2020gl088168

Wang, W., Shearer, P. M., Vidale, J. E., Xu, X., Trugman, D. T., & Fialko, Y. (2022). Tidal modulation of seismicity at the coso geothermal field. *Earth and Planetary Science Letters*, *579*, 117335. https://doi.org/10.1016/j.epsl.2021.117335

Weingarten, M., Ge, S., Godt, J. W., Bekins, B. A., & Rubinstein, J. L. (2015). High-rate injection is associated with the increase in us mid-continent seismicity. *Science*, *348*(6241), 1336–1340. https://doi.org/10.1126/science.aab1345

White, J. A., & Foxall, W. (2016). Assessing induced seismicity risk at co2 storage projects: Recent progress and remaining challenges. *International Journal of Greenhouse Gas Control*, *49*, 413–424. https://doi.org/10.1016/j.ijggc.2016.03.021

Zbinden, D., Rinaldi, A. P., Urpi, L., & Wiemer, S. (2017). On the physics-based processes behind production-induced seismicity in natural gas fields. *Journal of Geophysical Research: Solid Earth*, *122*(5), 3792–3812. https://doi.org/10.1002/2017jb014003

Zhai, G., Shirzaei, M., Manga, M., & Chen, X. (2019). Pore-pressure diffusion, enhanced by poroelastic stresses, controls induced seismicity in Oklahoma. *Proceedings of the National Academy of Sciences*, *116*(33), 16228–16233. https://doi.org/10.1073/pnas.1819225116

References From the Supporting Information

Borja, R. I. (2006). On the mechanical energy and effective stress in saturated and unsaturated porous continua. *International Journal of Solids and Structures*, *43*(6), 1764–1786. https://doi.org/10.1016/j.ijsolstr.2005.04.045

Duffield, G. (2007). Aqtesolv^{TM} version 4.5 user's guide.

McGarr, A. (2014). Maximum magnitude earthquakes induced by fluid injection. *Journal of Geophysical Research: Solid Earth*, *119*(2), 1008–1019. https://doi.org/10.1002/2013jb010597

Nakai, J., Sheehan, A., & Bilek, S. (2017b). Seismicity of the rocky mountains and rio grande rift from the EarthScope transportable array and CREST temporary seismic networks, 2008–2010. *Journal of Geophysical Research: Solid Earth*, *122*(3), 2173–2192. https://doi.org/10.1002/2016jb013389

Nakai, J., Weingarten, M., Sheehan, A., Bilek, S., & Ge, S. (2017c). A possible causative mechanism of Raton Basin, New Mexico and Colorado earthquakes using recent seismicity patterns and pore pressure modeling. *Journal of Geophysical Research: Solid Earth*, *122*(10), 8051–8065. https://doi.org/10.1002/2017jb014415

Qin, Y., Chen, T., Ma, X., & Chen, X. (2022). Forecasting induced seismicity in Oklahoma using machine learning methods. *Scientific Reports*, *12*(1), 9319. https://doi.org/10.1038/s41598-022-13435-3

Tariq, S. M. (1987). Evaluation of flow characteristics of perforations including nonlinear effects with the finite-element method. *SPE Production Engineering*, *2*(02), 104–112. https://doi.org/10.2118/12781-pa

Terzaghi, K., Peck, R. B., & Mesri, G. (1996). *Soil mechanics in engineering practice*. John wiley and sons.

Toda, S., Stein, R. S., & Sagiya, T. (2002). Evidence from the AD 2000 Izu islands earthquake swarm that stressing rate governs seismicity. *Nature*, *419*(6902), 58–61. https://doi.org/10.1038/nature00997

Van der Elst, N. J., Page, M. T., Weiser, D. A., Goebel, T. H., & Hosseini, S. M. (2016). Induced earthquake magnitudes are as large as (statistically) expected. *Journal of Geophysical Research: Solid Earth*, *121*(6), 4575–4590. https://doi.org/10.1002/2016jb012818

Wu, T. H. (1976). *Soil mechanics. Publication of*. Allyn and Bacon.